

1

Basic Principles of Capillarity in Relation to Crystal Growth

Nicolas Eustathopoulos
Laboratoire SIMaP

Béatrice Drevet
CEA-INES/RDI

Simon Brandon and Alexander Virozub
Technion–Israel Institute of Technology

The first part of this chapter (1.1) contains a brief definition of characteristic energies of surfaces and interfaces, as well as of capillary pressure. The second part (1.2) presents the basic principles of wettability and selected data for surface tension and contact angle for liquids of interest in crystal growth on various solid substrates. The third part (1.3) deals with growth angles, i.e. the contact angles formed by liquids on their own crystal, and the role of these angles in melt growth processes.

1.1 Definitions

1.1.1 Characteristic Energies of Surfaces and Interfaces

In order to define the characteristic energies of surfaces and interfaces, let us consider two bodies, solid (s) and liquid (l) respectively, that have a unit cross-sectional area. The

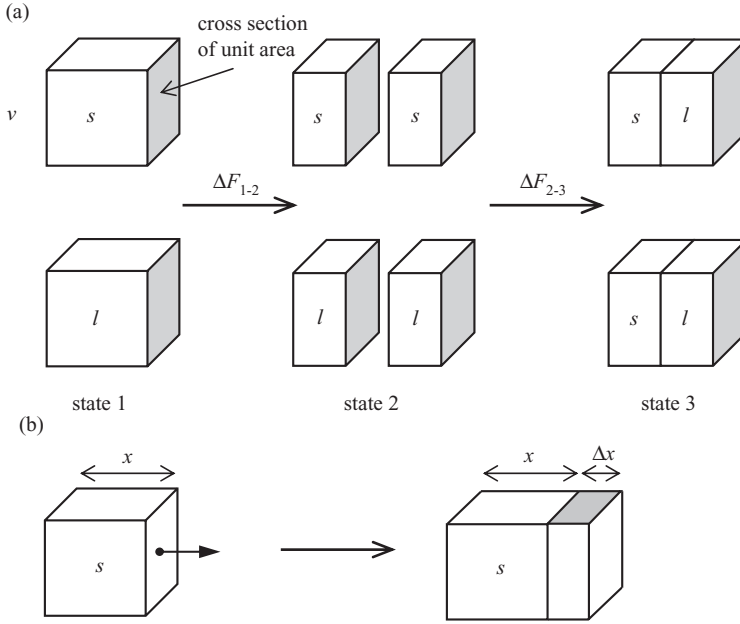


Figure 1.1 (a) Formation of two solid/liquid interfaces of unit area from pure solid and liquid bodies. (b) Formation of solid surface by elastic deformation.

solid and the liquid are surrounded by a vapour phase (v) at constant temperature. The free energy change corresponding to the reversible creation, without any elastic or plastic deformation, of two new surfaces of solid and liquid, by the process schematized in Figure 1.1.a, is:

$$\Delta F_{1-2} = 2(\gamma_{sv} + \gamma_{lv}) \quad (1.1)$$

In this expression, the quantities γ_{sv} and γ_{lv} define the surface energy of the solid and the liquid respectively. Consider now the transformation 2–3 consisting in joining two surfaces of solid and liquid. The free energy change is equal to:

$$\Delta F_{2-3} = 2(\gamma_{sl} - \gamma_{sv} - \gamma_{lv}) \quad (1.2)$$

Finally, the transformation 1–3 corresponds to:

$$\Delta F_{1-3} = \Delta F_{1-2} + \Delta F_{2-3} = 2\gamma_{sl} \quad (1.3)$$

where γ_{sl} is the solid/liquid interface energy.

For pure liquids and solids, the quantity $2\gamma_{lv}$ or $2\gamma_{sv}$ defines the *work of cohesion* W_c of the liquid ($W_c^l = 2\gamma_{lv}$) or the solid ($W_c^s = 2\gamma_{sv}$). The values of these quantities are proportional to the evaporation and sublimation energies per unit area respectively. In Equation

(1.2), the quantity $(\gamma_{sl} - \gamma_{sv} - \gamma_{lv})$ is equal but opposite in sign to the *work of adhesion* W_a defined by Dupré [Dupré 1869]:

$$W_a = \gamma_{sv} + \gamma_{lv} - \gamma_{sl} \tag{1.4}$$

Accordingly, the magnitude of W_a directly reflects the intensity of interactions between atoms in the liquid and solid states across the common interface.

1.1.2 Capillary Pressure

Consider a spherical liquid (l) drop of radius r in a vapour v. The volume of this drop is increased slowly, for instance by using a syringe to inject fresh liquid into the drop (Figure 1.2a). The increase of drop radius from r to $(r + dr)$ leads to an increase of the surface energy of the system equal to $d(4\pi r^2 \gamma_{lv}) = 8\pi r \gamma_{lv} dr$. If P_l is the pressure inside the drop and P_v the pressure in the vapour, the increase of r is associated with an amount of mechanical work to move the surface by a distance dr , i.e. $(P_l - P_v)4\pi r^2 dr$. Equating the two amounts of work leads to the expression of capillary pressure ΔP_c given by Laplace [Laplace 1805]:

$$\Delta P_c = P_l - P_v = 2 \gamma_{lv} / r \tag{1.5}$$

In the general case of a surface characterized by principal radii R_1 and R_2 (Figure 1.2.b), the curvature at each point Q of the liquid/vapour surface has to satisfy:

$$P_l^Q - P_v^Q = \gamma_{lv} \left(\frac{1}{R_1} + \frac{1}{R_2} \right) \tag{1.6}$$

The various mathematical forms of Laplace’s equation are discussed in Chapter 8. The capillary pressure ΔP_c preponderates over the hydrostatic pressure of a liquid of density ρ for liquid sizes less than a characteristic length called the *capillary length* and defined by $(\gamma_{lv}/(\rho g))^{1/2}$ where g is the acceleration due to gravity.

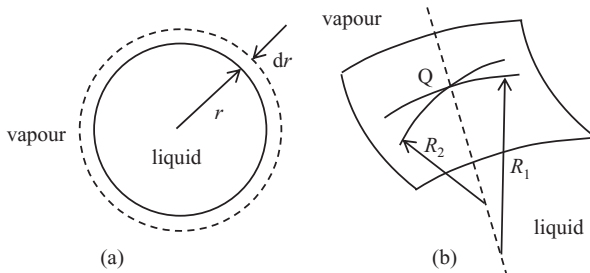


Figure 1.2 (a) Displacement of a liquid surface allowing derivation of the Laplace equation. (b) The principal radii of curvature R_1 and R_2 at a point Q on a curved liquid surface.

1.1.3 Surface Energy versus Surface Tension

In Figure 1.1.a, the two new solid/vapour surfaces are created by breaking bonds to increase the number of solid atoms (or molecules) which belong to the surface. A typical example of such a process is cleavage achieved without any elastic or plastic deformation of the solid. An alternative process to create a new solid/vapour surface is by purely elastic strain of the solid (Figure 1.1b), i.e. *without increasing the number of surface atoms*. The extra stress due to the surface, called ‘surface tension’ or ‘surface stress’, is denoted by σ_{sv} and expressed as a force per unit length.

For liquids, σ_{lv} and γ_{lv} are equal because the reversible stretching of a liquid surface is identical to the reversible creation of new surface. In both cases, the liquid can increase its surface area only by the addition of new atoms to the surface. Note that, from a dimensional point of view, an energy per unit area is equivalent to a force per unit length and the values are numerically equal when γ_{lv} is measured in Jm^{-2} and σ_{lv} is measured in Nm^{-1} .

For solids, σ_{sv} and γ_{sv} are different quantities. For instance, for each crystal face, there is a unique value of γ_{sv} (which is a scalar) while σ_{sv} depends also on the orientation along the face. Moreover, γ_{sv} is always a positive quantity (breaking bonds needs work) while σ_{sv} can be either positive or negative [Nolfi 1972]. For high symmetry surfaces, the surface tension is related to the surface energy by the equation [Shuttleworth 1950]:

$$\sigma_{sv} = \gamma_{sv} + d\gamma_{sv}/d\varepsilon \quad (1.7)$$

where ε is a macroscopic elastic strain. The physical origin of the difference between γ_{sv} and σ_{sv} , i.e. of the term $d\gamma_{sv}/d\varepsilon$ in Equation (1.7), can be explained taking into account the atomistic origin of γ_{sv} . For instance, for monoatomic solids, γ_{sv} is proportional to the difference in potential energy between an atom of the surface and an atom of the bulk solid. When a new surface is created by stretching the solid (Figure 1.1b), this difference does not remain constant. Indeed, because surface atoms are bonded weakly compared to those in the bulk, the work needed to stretch the surface is less than for the bulk material.

From now on, for solid/vapour and solid/liquid boundaries, only the surface and interface energies γ_{sv} and γ_{sl} will be considered. For liquid/vapour boundaries, both the surface tension σ_{lv} and surface energy γ_{lv} will be used interchangeably depending on the context.

1.2 Contact Angles

In this part (sections 1.2.1–1.2.4), the fundamental equations describing the wetting of ideal surfaces in chemically inert systems are given. Then the wetting of real surfaces is presented, taking into account the effects of roughness and chemical heterogeneities of the solid surface. The dynamics of wetting will be presented mainly for nonreactive solid/liquid systems and more briefly for reactive ones. After a short description of methods for measuring contact angles and surface tensions at high temperature, selected data are

given and discussed for molten semiconductors, oxides and halides on solid oxides, carbon, nitrides and metallic substrates.

1.2.1 Thermodynamics

1.2.1.1 Ideal Solid Surfaces

Young's and Young–Dupré equations. Consider a flat, undeformable, perfectly smooth and chemically homogeneous solid surface in contact with a nonreactive liquid in the presence of a vapour phase. If the liquid does not completely cover the solid, the liquid surface will intersect the solid surface at a 'contact angle' θ . The equilibrium value of θ , used to define the wetting behaviour of the liquid, obeys the classical Young's equation [Young 1805]:

$$\cos\theta_Y = \frac{\gamma_{sv} - \gamma_{sl}}{\gamma_{lv}} \quad (1.8)$$

In this chapter, a contact angle of less than 90° will identify a wetting liquid, while a greater value will identify a nonwetting liquid. If the contact angle is zero, the liquid will be considered to be perfectly wetting.

Equation (1.8) can be easily derived by calculating the variation of the *surface* free energy F_s of the system caused by a small displacement δx of the solid/liquid/vapour *triple phase line* (TPL). In Figure 1.3, the TPL is perpendicular to the plane of the figure and assumed to be a straight line, rendering the problem two-dimensional. Thus, the total length of the TPL is constant during its displacement, as in the case of a meniscus formed on a vertical plate. Moreover, the radius r of the TPL region considered in this derivation (Figure 1.3) is much larger than the range of atomic (or molecular) interactions in the

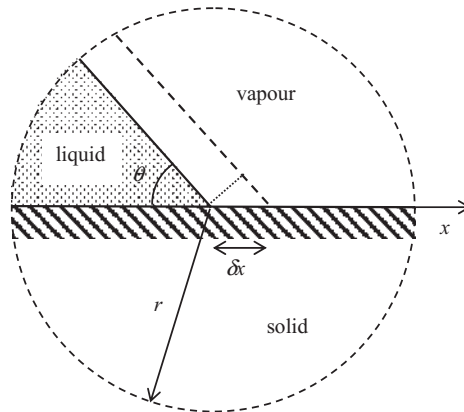


Figure 1.3 Displacement of a triple line around its equilibrium position that allows derivation of Young's equation. Only a small region close to the triple line is taken into account to neglect the curvature of the liquid/vapour surface.

system ($r \gg 10 \text{ nm}$) and small compared to a characteristic dimension of the liquid, for instance the average drop base radius R in the sessile drop configuration (see Figure 1.15a) or the maximum height of a meniscus formed on a vertical solid wall which are both typically in the millimetre range. With these assumptions, the variation of interfacial free energy per unit length of the TPL, resulting from a small linear displacement δx of the TPL, is

$$F_s(x + \delta x) - F_s(x) = \delta F_s = (\gamma_{sl} - \gamma_{sv})\delta x + \cos(\theta)\gamma_{lv}\delta x$$

and the equilibrium condition $d(\delta F_s)/d(\delta x) = 0$ leads to Equation (1.7). Young's equation was shown also to be valid in the presence of the gravitational field for the configuration of a meniscus formed on a vertical plate [Neumann 1972, Eustathopoulos 1999 p. 12], and for the classical configuration of an axisymmetric sessile drop [Garandet 1998].

By combining Equation (1.4) of W_a and the Young Equation (1.8), the following fundamental equation of wetting, known as the Young–Dupré equation, is obtained:

$$\cos \theta = \frac{W_a}{\gamma_{lv}} - 1 \quad (1.9)$$

Taking into account the transformation ΔF_{3-2} of Figure 1.1a, this equation shows that the contact angle results from the competition of two types of forces: cohesion forces responsible for γ_{lv} ($\gamma_{lv} = W_c/2$) and adhesion forces responsible for W_a .

System Size Effects. In the sessile drop configuration, the increase of the drop base radius during wetting leads not only to a change of surface and interface areas but also to the increase of the TPL length. The TPL can be considered as a line defect, similar to the step energy in crystal growth, with a specific excess energy τ [Eustathopoulos 1999 p. 10]. Therefore, the contact angle is in principle a function not only of surface energies γ_{ij} but also of τ . However, the importance of τ decreases when the drop size increases, and becomes negligible for a droplet radius of more than a few tens of nm [Chizhik 1985, Eustathopoulos 1999 p. 11].

Metastable and Stable Contact Angles. Young's equation is derived from minimization of the free energy of the system carried out by considering only displacements of the triple line parallel to a solid/vapour surface assumed to be undeformable (Figure 1.4b). Therefore, θ_Y corresponds to a metastable equilibrium configuration. For isotropic solid/vapour and solid/liquid surface and interfacial energies, the local stable equilibrium shown in Figure 1.4c is described by the Smith equation by means of three dihedral angles θ_l , θ_v and θ_s [Smith 1948]:

$$\frac{\gamma_{sv}}{\sin \theta_l} = \frac{\gamma_{sl}}{\sin \theta_v} = \frac{\gamma_{lv}}{\sin \theta_s} \quad (1.10)$$

For a simple derivation of this equation, the interested reader can refer to [Eustathopoulos 1999 p. 16].

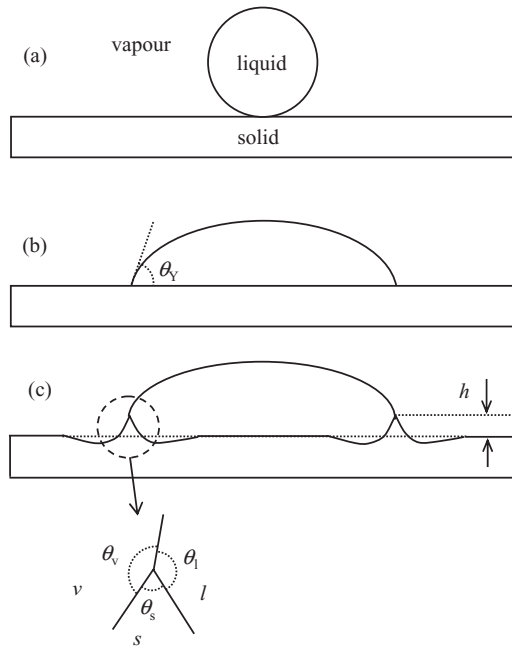


Figure 1.4 Metastable (b) and stable (c) equilibrium angles at a solid/liquid/vapour junction obtained after spreading of a liquid droplet (a).

For fluids with low viscosity (a few mPa s), such as molten metals and semiconductors or certain oxide melts at high temperature, the approach to the local stable equilibrium occurs in two stages with very different rates. In the first rapid stage (spreading time for millimetre-sized droplets of the order of 10^{-1} or 10^{-2} s, see section 1.2.2.1), the macroscopic contact angle approaches θ_Y . This stage is followed by a much slower process occurring at the vicinity of the triple line to satisfy the Smith equation. As discussed in [Saiz 1998], the growth of the ‘wetting ridge’ of height h (Figure 1.4c) can take place by mechanisms similar to those occurring during grain boundary grooving as described by Mullins [Mullins 1957, 1960]. An example is millimetre-size Cu droplets on Al_2O_3 surfaces in Ar at 1150°C . While the Young contact angle is reached in a few ms, a wetting ridge with $h = 10$ nm is formed after 2 h. Clearly, such a wetting ridge has a negligible effect on the value of the contact angle. Therefore, the area of the solid/liquid and liquid/vapour interfaces at equilibrium is determined essentially by the value of θ_Y .

For vitreous solids, such as SiO_2 , viscosity decreases strongly close to the melting point. In this case, the solid ridge can be formed by viscous flow and the height h can reach easily measurable sizes in quite short times. For example, wetting of a Ni droplet on a SiO_2 substrate at 1470°C is accompanied by the formation, in about 20 min, of an easily observable SiO_2 meniscus on the Ni drop ($h = 5\text{--}10\ \mu\text{m}$) [Merlin 1992].

1.2.1.2 Effect of Roughness

The roughness of solid surfaces affects wetting as a result of two different effects: the first is the fact that the actual surface area is increased and the second is pinning of the triple line by sharp edges.

Effect of Increased Surface Area – Wenzel Equation. If s_r denotes the ratio of the actual area to the planar area ($s_r > 1$), for a surface with a small asperity wavelength compared to the capillary length, the macroscopic equilibrium contact angle denoted by θ_w is given by the equation of Wenzel [Wenzel 1936]:

$$\cos \theta_w = s_r \cos \theta_Y \quad (1.11)$$

According to this equation, for $\theta_w < 90^\circ$ and if $s_r > 1/\cos \theta_w$, perfect wetting will be observed.

Effect of Sharp Edges – Hysteresis of Contact Angle. Sharp edges can pin the triple line at positions far from stable equilibrium, i.e. at contact angles markedly different from θ_Y . This effect is illustrated schematically in Figure 1.5 where a solid substrate with an horizontal surface A_1 and another surface A_2 inclined at an angle β is considered. The initial equilibrium configuration of the liquid surface, marked (1) in Figure 1.5, corresponds to a contact angle on the A_1 surface $\theta(A_1) = \theta_Y$. Then, if the liquid volume is increased slowly enough for the liquid to retain capillary equilibrium, the TPL will advance on surface A_1 and reach configuration (2) where the contact angle at point N is $\theta_N(A_1) = \theta_Y$. Thereafter, the TPL will be pinned at point N and the macroscopic contact angle on A_1 , $\theta_N(A_1)$, will increase until the liquid surface assumes configuration (3) where $\theta_N(A_1) = \theta_Y + \beta$, which corresponds to the establishment of the Young contact angle on the A_2 surface, i.e. $\theta_N(A_2) = \theta_Y$. Any further increase in the liquid volume will produce a movement of the TPL on the A_2 surface, for example to configuration (4) with $\theta(A_2) = \theta_Y$.

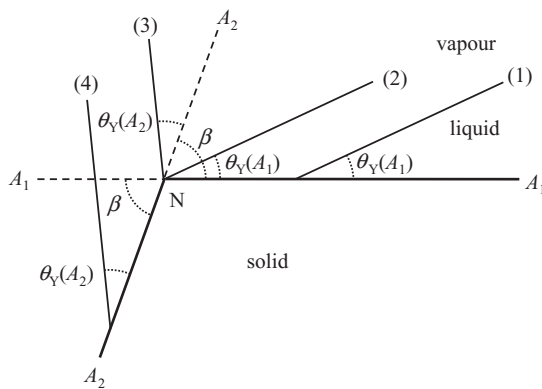


Figure 1.5 Effect of a sharp edge on the contact angle when a triple line advances on a solid surface. (1), (2), (3) and (4) denote the successive configurations of the liquid surface when the liquid volume is increased.

Thus, the liquid can form an infinite number of *advancing* contact angles at point N on the A_1 surface lying between θ_Y and $\theta_Y + \beta$. This last value defines the maximum advancing contact angle on A_1 :

$$\theta_a(\max) = \theta_Y + \beta \tag{1.12a}$$

Consider now that configuration (4) in Figure 1.5 represents the initial liquid surface and that the liquid volume is slowly decreased. Using similar arguments for the retreat of the liquid on the A_2 surface, it can be shown that the liquid can form an infinite number of *receding* contact angles at point N on the A_2 surface lying between θ_Y and $\theta_Y - \beta$. This last value defines the minimum receding contact angle on A_2 :

$$\theta_r(\min) = \theta_Y - \beta \tag{1.12b}$$

When these considerations are applied to a rough surface consisting of grooves parallel to the moving triple line, one can identify the maximum advancing contact angle and the minimum receding contact angle, as shown in Figure 1.6:

$$\theta_a(\max) = \theta_Y + \beta_{\max} \tag{1.13a}$$

$$\theta_r(\min) = \theta_Y - \beta_{\max} \tag{1.13b}$$

The range of angles lying between $\theta_a(\max)$ and $\theta_r(\min)$ defines the hysteresis domain of contact angle. For a given system and roughness, a large number of angles belonging to the hysteresis domain and corresponding to metastable equilibrium states can be observed. Vibrations help the triple line to overcome the energy barriers caused by roughness and to approach the stable equilibrium state, i.e. the Wenzel contact angle (Equation (1.11)). In practice, for random roughness surfaces with average roughness parameter R_a of about 100nm, the excess $(\theta_a - \theta_Y)$ values are a few degrees, while for R_a close to 1 μm the excess $(\theta_a - \theta_Y)$ values for various nonwetting liquids can be as much as 20° [Hitchcock 1981, Eustathopoulos 2005] (Figure 1.7).

Composite Wetting. For solid surfaces with high roughness, a liquid forming large nonwetting contact angles ($\theta \gg 90^\circ$) cannot infiltrate surface cavities, resulting in the

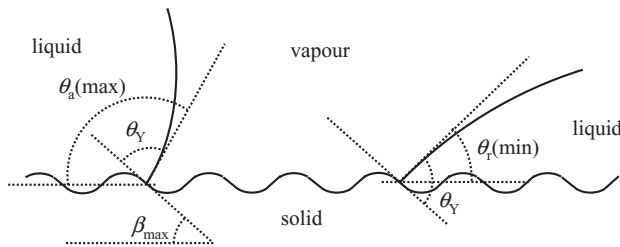


Figure 1.6 Identification of the maximum advancing contact angle $\theta_a(\max)$ and minimum receding contact angle $\theta_r(\min)$ on a rough surface.

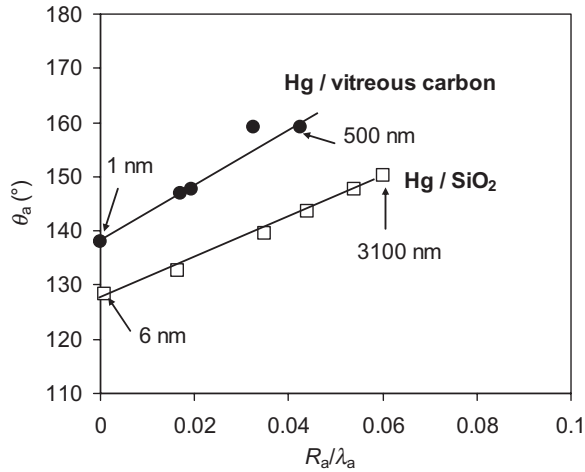


Figure 1.7 Advancing contact angle θ_a measured by the sessile drop technique as a function of R_a/λ_a , a quantity proportional to the average slope of the surface profile where R_a is the average roughness and λ_a the average wavelength of the asperities, for Hg on abraded SiO_2 and C_v ; the arrows indicate R_a values. θ_v values for Hg on these substrates are the values at $R_a/\lambda_a = 0$ [Eustathopoulos 2005a]. Data from work reported in [Hitchcock 1981].

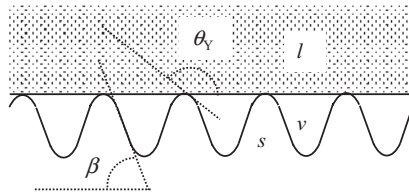


Figure 1.8 Formation of a composite interface in a nonwetting system.

formation of a composite interface, i.e. a mixed solid/liquid interface and solid/vapour surface (Figure 1.8). A characteristic of such an interface is the disappearance of the energy barriers to the movement of the TPL. Indeed, the liquid surface contacts the solid only at a limited number of points so that no pinning of the TPL can occur, explaining why the difference $(\theta_a - \theta_r)$ tends towards zero in this case. Thus, Hg droplets on ceramic surfaces are very mobile. Indeed, owing to the poor wetting by Hg and the formation of composite interface, droplets are never pinned and move easily.

The condition for the transition from a solid/liquid to a composite interface is given by [Eustathopoulos 1999 p. 34]:

$$\beta > 180^\circ - \theta_v \tag{1.14}$$

where β is the maximal average slope of the surface. In practice, θ_v values of metals and semiconductors are rarely greater than 150° . In this case, composite interfaces can be obtained only with very rough surfaces ($\beta > 30^\circ$).

Sticking. When composite interfaces are formed, no sticking is observed during cooling at room temperature, whatever the thermomechanical characteristics of the system. Typical examples are nonreactive metals (e.g. Cu, Ag) on polycrystalline graphite, or soda-lime glasses on steel moulds lubricated with a porous layer of carbon [Pech 2005].

When a true interface is established at any point of the common area, the behaviour of the interface on cooling depends on several material parameters, as well as system geometry and cooling rate. Sticking is favoured by (i) a high adhesion energy W_a and (ii) a low thermoelastic energy stored in the system during cooling due to thermal contraction mismatch ($\Delta\alpha = \alpha_A - \alpha_B$) between the substrate A and the solidified liquid B. For a given $\Delta T = T_{\text{sol}} - T_{\text{room}}$ (where T_{sol} is the temperature of solidification and T_{room} the room temperature), this energy increases proportionally to $(\Delta\alpha)^2$ and to $E_A E_B^2 / (E_A + E_B)^2$ where E is Young's modulus [Pech 2004]. Ductility of one of the contacting phases in a certain range of temperature contributes to decrease, by plastic deformation, the driving force for detachment. Many semiconductors (e.g. Si, InSb, GaSb) are brittle materials, such that energy dissipation by plastic deformation is small. In this case, the mechanical response of the system during cooling depends critically on the adhesion energy of the solidified liquid/substrate couple. For instance, for Si on Si_3N_4 and SiC, the adhesion energy is high (Si wets well both these ceramics; see Tables 1.4 and 1.5) resulting in sticking or cohesive fracture [Drevet 2009]. Conversely, the adhesion energy of GaSb and InSb on vitreous carbon is very low (see Table 1.4) leading during cooling to detachment by a purely interfacial separation [Harter 1993, Boiton 1999]. See also Chapter 6, section 6.1.3.

1.2.1.3 Wetting on Heterogeneous Surfaces

Many materials of practical interest are multiphase solids with heterogeneous surfaces that can be either regular (oriented eutectics, unidirectional composites, etc.) or random ('hard' alloys processed by liquid phase sintering, alloys strengthened by precipitation, etc.).

Consider an horizontal solid consisting of two macroscopic phases α and β separated by a plane intersecting the solid surface by a vertical straight line (Figure 1.9). The intrinsic contact angles on the two phases are such that $\theta_\alpha > \theta_\beta$, and for the sake of clarity $\theta_\alpha > 90^\circ$ and $\theta_\beta < 90^\circ$. The initial position of the liquid surface is on the β phase with a macroscopic contact angle θ_M equal to θ_β (configuration (1) on Figure 1.9). If the liquid volume is increased, when the TPL reaches the line of separation from β to α , it will be pinned at this position by the nonwetted α phase (configuration (2)). When the volume of the liquid is increased again, the TPL does not move until configuration (3) is obtained

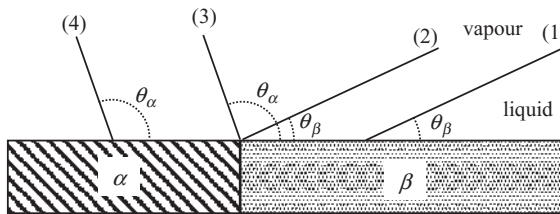


Figure 1.9 Successive configurations of the liquid surface on a solid surface consisting of two macroscopic phases α and β when the liquid volume is increased.

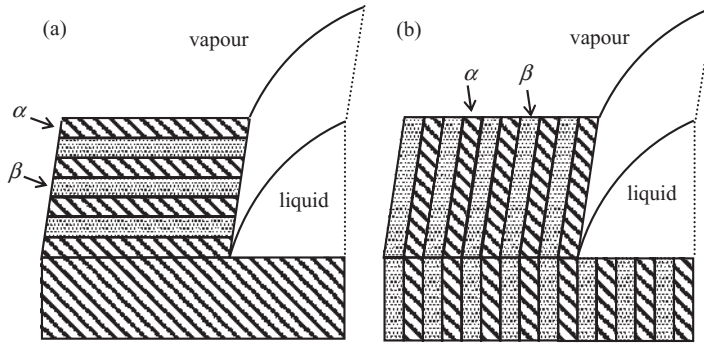


Figure 1.10 Composite solid consisting of alternate strips perpendicular (a) and parallel (b) to the triple line.

where $\theta_M = \theta_\alpha$. If the liquid volume is further increased, the TPL will move on the α surface while θ_M will remain equal to θ_α (configuration (4)).

Consider now the case of a composite solid consisting of alternate strips of α and β phases, with contact angles θ_α and θ_β , such that the surface area fractions are f_α and f_β . The width of the strips is assumed small compared to the capillary length, so that the macroscopic TPL is a straight line which is either perpendicular (Figure 1.10a) or parallel (Figure 1.10b) to the strips. For the first situation, it has been shown that there are no metastable states and, as a consequence, no hysteresis of contact angle [Johnson 1993, Neumann 1972]. The macroscopic contact angle that would be observed at equilibrium, denoted θ_C , is then given by Cassie's equation [Cassie 1948]:

$$\cos \theta_C = f_\alpha \cos \theta_\alpha + (1 - f_\alpha) \cos \theta_\beta \quad (1.15)$$

This equation, which is an analog of the Wenzel equation for rough surfaces (Equation (1.11)), gives the stable equilibrium contact angle for any heterogeneous surface.

When the TPL is parallel to the strips, a situation analogous to a rough surface with grooves parallel to the TPL (Figure 1.6), free energy change calculations [Johnson 1993, Neumann 1972] indicate the existence of metastable states separated by energy barriers for any position of the TPL corresponding to a macroscopic contact angle θ_M between θ_α and θ_β . Consequently, the maximum advancing and minimum receding contact angles are given by the equations:

$$\theta_a(\max) = \theta_\alpha \quad (1.16a)$$

$$\theta_r(\min) = \theta_\beta \quad (1.16b)$$

which are analogous to equations (1.13) for rough surfaces.

1.2.2 Dynamics of Wetting

In this section, spreading kinetics will be presented first for nonreactive solid/liquid systems and then for reactive ones. In view of the systems of interest in crystal growth,

the reactive case will be presented briefly. Nonreactive systems exhibit a reactivity low enough such that the resulting solid/liquid interface remains flat at the macroscopic scale and reactivity has a negligible effect on the interfacial energies. Under this last condition, interfacial energies can be taken constant with time during the wetting process.

1.2.2.1 Nonreactive Spreading

Consider a drop of millimetre size spreading on a flat surface spontaneously, i.e. in the absence of any external force. The triple line velocity $U = dR/dt$, where R is the drop base radius, results from a balance of forces that drive and resist to spreading. The driving force for wetting per unit length of triple line is given by the change in the surface and interfacial energies of the system resulting from a lateral displacement of the triple line:

$$\gamma_{sv} - \gamma_{sl} - \gamma_{lv} \cos \theta = \gamma_{lv} (\cos \theta_F - \cos \theta) \quad (1.17)$$

where θ_F is the final, equilibrium, contact angle. In the so-called hydrodynamic models of wetting, energy dissipation is supposed to occur by viscous friction in a macroscopic wedge near the triple line of typical width 0.1 mm. The resulting expression for U for $\theta < 135^\circ$ is:

$$U = \frac{\gamma_{lv}}{\mu K} (\theta^3 - \theta_F^3) \quad (1.18)$$

where μ is the dynamic viscosity, K is a constant close to 100 and θ is expressed in radians [de Gennes 1985, Cox 1986, Kistler 1993]. It has been shown that this equation does not depend on the configuration (sessile drop or meniscus formed on a vertical wall). Moreover, this equation is valid for both spontaneous and forced spreading. An example of forced spreading is the steady immersion (or withdrawal) of a plate in a liquid bath at an *imposed rate* U . Then, the observed contact angle would be the value $\theta(U)$ given by Equation (1.18). Finally, for θ_F close to zero, Equation (1.18) can be written as:

$$\theta \equiv \left(\frac{K\mu U}{\gamma_{lv}} \right)^{1/3} = K^{1/3} Ca^{1/3} \quad (1.19)$$

where Ca is the capillary number. Accordingly, for all liquids with $\theta_F \equiv 0$, the experimental $\theta = f(Ca)$ results would lie on the same ‘universal’ curve.

Molten metals and semiconductors are low viscosity liquids, their viscosity close to the melting point being a few mPas. For this type of liquid, the experimental average U is very high, of the order of 1 m s^{-1} . For millimetre-sized droplets, this leads to spreading times t_s of a few ms [Eustathopoulos 1999 p. 54]. The analysis of experimental results obtained in the sessile drop configuration shows that values $U(\theta)$ predicted by Equation (1.18) consist in an upper limit. Overestimation of U is particularly high for $\theta > 30^\circ$. For instance, in the liquid Sn/solid Ge system at 600° in which the final contact angle is about 40° [Naidich 1992], the spreading rate at $\theta = 80^\circ$ is about 0.5 m s^{-1} , while the value calculated by Equation (1.18), taking $\gamma_{lv} = 0.5 \text{ J m}^{-2}$ and $\mu = 1.1 \text{ mPas}$, is 11 m s^{-1} . For low viscosity liquids and large θ , it is likely that the spreading rate is limited not by viscous

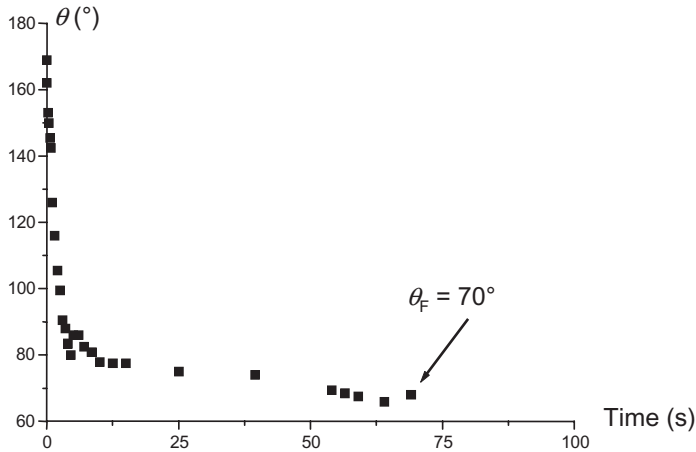


Figure 1.11 Wetting kinetics of a drop of soda-lime glass (13.4 wt% Na_2O , 10.9 wt% CaO , 1.6 wt% Al_2O_3 , 1.4 wt% MgO , SiO_2 bal.) on steel at 1200°C ($\mu = 10^2 \text{ Pa s}$) [J. Pech, M. Jeymond, N. Eustathopoulos, unpublished work].

flow but by the movement of atoms at the solid/liquid interface close to the triple line, as proposed by Blake [Blake 1993], who considered spreading as an adsorption–desorption process of the liquid atoms on the substrate surface. The values of U calculated by Blake’s model are very sensitive to the value of a model parameter, i.e. the activation energy of wetting which is an unknown quantity.

The viscosity of molten oxides is often several orders of magnitude greater than that of molten metals. As a consequence, the spreading time t_s for millimetre-sized droplets can attain several seconds or hundreds of seconds (vs a few ms for metals) and even more. In agreement with Equation (1.18), the wetting rate is very high at short times (i.e. for high θ values) and decreases strongly at longer times (Figure 1.11). Finally, the experimental wetting curves obtained for the same molten oxide/solid metal couple by varying the temperature by 240° (implying a variation of μ by more than two orders of magnitude) are plotted as $\theta = f(\text{Ca})$ on Figure 1.12. In agreement with Equation (1.18), a unique curve is obtained (note that in these experiments the change of θ_F with temperature is negligible) [Pech 2004].

1.2.2.2 Reactive Spreading

In this type of spreading, wetting is accompanied by (and in many cases coupled to) a reaction forming a new compound at the interface. The fundamentals of reactive wetting (driving force, limiting process) have been studied mainly for molten metals and alloys on ceramics and are reviewed in [Eustathopoulos 2005b]. In these systems, the observed spreading times are in the range 10^1 – 10^3 s (Figure 1.13), corresponding to spreading rates U several orders of magnitude lower than those measured for molten metals in nonreactive spreading. Therefore, in reactive spreading, U is limited by the interfacial reaction itself. Actually it has been shown that the relevant region is not the two-dimensional solid/liquid interface but the solid/liquid/vapour triple line. Indeed, at this line where the liquid

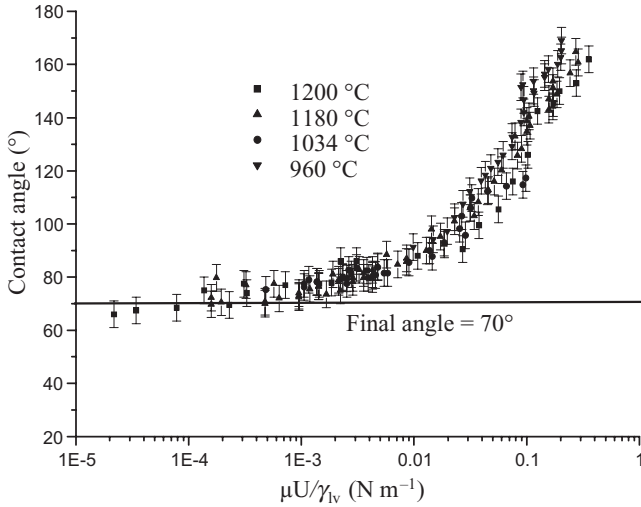


Figure 1.12 Contact angle as a function of $Ca = \mu U/\gamma_{lv}$ for the glass 13.4 wt% Na_2O , 10.9 wt% CaO , 1.6 wt% Al_2O_3 , 1.4 wt% MgO , bal. SiO_2 on steel at different temperatures (Reprinted with permission from [Pech 2004], copyright (2004) Elsevier Ltd).

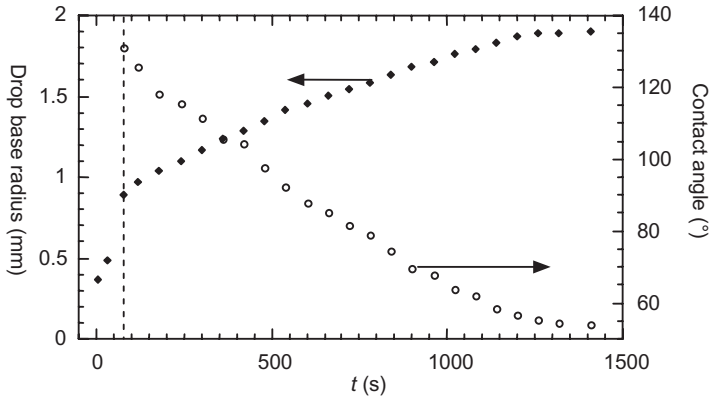


Figure 1.13 Variation of drop base radius and contact angle with time for Ge-20 at.% Si alloy on vitreous carbon at 1231°C under high vacuum (the dashed vertical line indicates the moment of drop detachment from the capillary end in the dispensed drop apparatus of Figure 1.15b) (Reprinted with kind permission from [Dezellus 2000], copyright (2000) O. Dezellus). In this system, wetting is promoted by the formation at the interface of a wettable SiC layer.

contacts directly a fresh surface of the solid substrate, the growth rate of the reaction product is maximal (Figure 1.14). Far behind the triple line, thickening of the reaction product continues but this process is slow as it occurs by solid state diffusion. Two regimes of reactive spreading have been identified depending on the relative rate of the two successive steps: (i) diffusion of the reactive solute from the liquid bulk to the triple

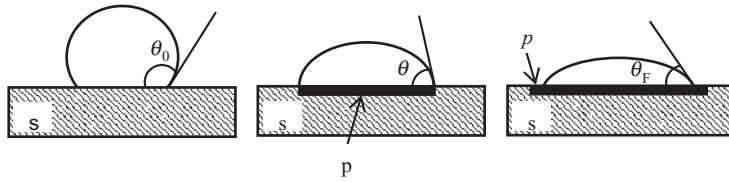


Figure 1.14 Schematic representation of the ‘reaction product control’ model. The initial contact angle θ_0 is the contact angle on the unreacted ceramic substrate surface s . After a transient stage, a quasi-state configuration is established at the triple line where the advance of the liquid is hindered by the presence of a nonwetable substrate in front of the triple line. Thus, the only way to move ahead is by lateral growth of the wettable reaction product layer p until the macroscopic contact angle equals the equilibrium contact angle θ_F of the liquid on the reaction product (Reproduced with permission from [Eustathopoulos 1998], copyright (1998) Elsevier Ltd).

line and (ii) the local process at the triple line. When the local process at the triple line is the slowest one, the spreading rate U was found to be nearly constant in a large domain of the $\theta(t)$ curve (linear spreading) (Figure 1.13). Conversely, nonlinear spreading is predicted for diffusion controlled reactive spreading (drop base radius $R \sim t^{1/4}$) [Mortensen 1997].

1.2.3 Measurements of Contact Angle and Surface Tension by the Sessile Drop Technique

A critical review of the state of knowledge in high temperature contact angle measurement is given in [Eustathopoulos 1999 p. 106, Eustathopoulos 2005a]. Briefly, the technique most widely used for wetting experiments is the sessile drop method. In its classical form, shown in Figure 1.15a, a small piece of solid, typically some tens or hundreds of milligrams, is placed on a substrate and then heated above its melting temperature. In another variant, a metal or alloy is melted in an unwetted and chemically inert ceramic tube and is dispensed on the substrate surface through a small hole in the tube end by applying a back pressure of inert gas or using a piston (Figure 1.15b). One advantage of this technique is that oxide films on liquid metals are disrupted during liquid extrusion from the crucible through the capillary. In the ‘transferred drop’ technique (Figure 1.15c), a sessile drop can be melted on an inert substrate, which is then raised so that the top of the drop contacts a fresh solid surface. The liquid can be transferred to the top substrate provided it is better wetted than the inert bottom substrate. In all the above techniques, values of advancing contact angles θ_a are measured and they are attained by an irreversible movement of the triple line from $\theta \sim 180^\circ$ to θ_a .

When it is possible, single crystal or amorphous substrates with a random roughness less than 100 nm are preferred in order to achieve an acceptable accuracy of θ (a few degrees). The experiments are conducted in controlled furnace conditions under either high vacuum or gases with low or known oxygen partial pressure. For contact angles greater than 90° , the sessile drop technique allows the surface tension of the liquid to be determined with an accuracy of 2–3% by fitting the shape of the droplet to the Laplace

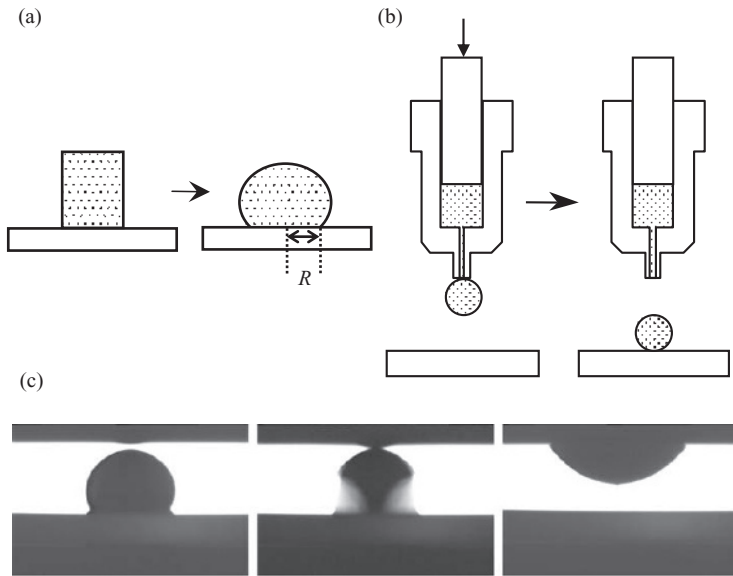


Figure 1.15 (a) Classical sessile drop method. (b) Dispensed drop method. (c) Example of the transferred drop method: Pb drop transferred from an Al_2O_3 substrate (bottom) to a Fe substrate (top) at 400°C .

equation, i.e. by expressing at each point of the drop surface the balance between the hydrostatic pressure and the capillary pressure. This is often performed by automatic imaging procedures that give also a reliable value of the contact angle. Table 1.1 gives the value of γ_v for a number of semiconductors and compounds relevant in crystal growth.

1.2.4 Selected Data for the Contact Angle for Systems of Interest for Crystal Growth

1.2.4.1 Semiconductor/Ceramic Systems

Semiconductors on Oxides. The wettability of ionocovalent oxides by molten metals and semiconductors depends critically on their reactivity at the common interface. This can be quantified by the molar fraction of oxygen in the liquid metal, X_O^l , provided by the dissolution of the oxide at the solid/liquid interface I. For SiO_2 , the dissolution reaction is:



where the parentheses mean that the species are in the liquid state. It has been found in [Eustathopoulos 1998, Eustathopoulos 1999 p. 198] that for all metal/oxide couples with $X_O^l < 10^{-5}$, the observed equilibrium contact angles are in the range $115\text{--}135^\circ$ whatever the value of X_O^l . In these systems, considered as nonreactive from the point of view of

Table 1.1 Values of surface tension for compounds of interest in crystal growth

Compound	T_m (°C)	γ_v (mJm ⁻²)	Reference
Ge	937	587–0.105 ($T - T_m$)	[Eustathopoulos 1999 p. 149]
Si ^a	1412	827–0.48 ($T - T_m$) 749–0.15 ($T - T_m$)	[Eustathopoulos 1999 p. 149]
GaSb	711	453–0.14 ($T - T_m$)	[Harter 1993]
InSb	530	434–0.08 ($T - T_m$)	[Harter 1993]
CdTe	1092	181 at T_m $d\gamma_v/dT = -0.16$	[Shetty 1990a]
Pb _{0.8} Sn _{0.2} Te	$T_l = 905$	186 at 1100°C	[Katty 1992]
GaAs	1238	230–0.17 ($T - 905$ °C) 465 at T_m $d\gamma_v/dT = -0.96$	[Kinoshita 1989] [Shetty 1990b]
Al ₂ O ₃	2047	630 at T_m	[Eustathopoulos 1999 p. 165]
SiO ₂	1720	307 at T_m	[Eustathopoulos 1999 p. 165]
CaF ₂	1418	387 at T_m	[Tanaka 1996]
BaF ₂	1290	253 at T_m	[Tanaka 1996]
LiF	848	236 at T_m	[Tanaka 1996]
NaF	992	186 at T_m	[Tanaka 1996]
CsI	621	72 at T_m	[Tanaka 1996]
NaI	660	86 at T_m	[Tanaka 1996]
LiNbO ₃	1250	192 at 1300°C	[Shi 1980]

T_l , temperature of liquidus; T_m , melting temperature.

^aTwo groups of values for both $\gamma_v(T_m)$ and $d\gamma_v/dT$ have been found.

wettability, adhesion is ensured mainly by weak, van der Waals, interactions. Typical examples are the noble metals Ag, Au, Cu and the low melting point metals Ga, In, Pb, Sn on SiO₂ or Al₂O₃ substrates. Note that for these systems, the contact angle decreases with temperature only slightly ($d\theta/dT \cong 10^{-2}/K$). The molten Ge/SiO₂ couple in high vacuum belongs to this type of system (Table 1.2).

For a given metal/oxide couple, the concentration of oxygen in the liquid metal can be increased above the value imposed by the interfacial equilibrium (1.20) by increasing the oxygen partial pressure P_{O_2} in the furnace atmosphere. Indeed, according to Henry's law (i.e. constant activity coefficient of the diluted solute), at constant temperature $X_O = K(T)P_{O_2}^{1/2}$, where $K(T)$ is a constant depending on the metal. As shown in Figure 1.16, when X_O becomes higher than $X_O^w \cong 10^{-5}$, the contact angle decreases from its 'plateau' value, and for elements such as Ag, Cu or Ni dissolving enough oxygen, contact angles as low as 80–100° have been observed on Al₂O₃. A similar 'wetting transition' was found for molten Pb on SiO₂ [Sangiorgi 1995]. As discussed in [Naidich 1981, Eustathopoulos 1999 p. 220, Eustathopoulos 2001], the improvement of wetting by dissolved oxygen results from the development of chemical interactions between the oxide surface and oxygen–metal clusters formed in the liquid.

Oxidation of the liquid metal M surface can occur when P_{O_2} in the furnace becomes equal to $P_{O_2}^{ox}$ corresponding to the reaction $(M) + n/2[O_2] \rightarrow <MO_n>$. When the MO_n oxide is solid, the skin formed around the metal prevents direct contact between the liquid and the substrate resulting in very large, obtuse, contact angles (typically 150–160°) (Figure 1.16). As long as such oxide skins exist, no sticking is observed on cooling.

Table 1.2 Contact angle of semiconductors on SiO₂

Semiconductor	T (°C)	Atmosphere	θ_F (°)	Reference
Ge	1100	High vacuum	115	[Kaiser 2001]
		Ar	155	
Si	1420	Ar ($P_{O_2} = 10^{-15}$ Pa)	85	[Yuan 2004]
Ge-4.6 at.% Si	1100	High vacuum	105	[Cröll 2002]
Ge-10.7 at.% Si			100	
GaSb	920	High vacuum	119	[Harter 1993]
GaSb	710–910	H ₂	132	[Cröll 2003]
InSb	800	High vacuum	110	[Harter 1993]
InP	1065	High vacuum + P vapour	140–150	[Shimizu 2002]
GaAs	1238	High vacuum + As vapour	115	[Shetty 1990b]
CdTe	1092	High vacuum + Cd vapour	83	[Shetty 1990a]

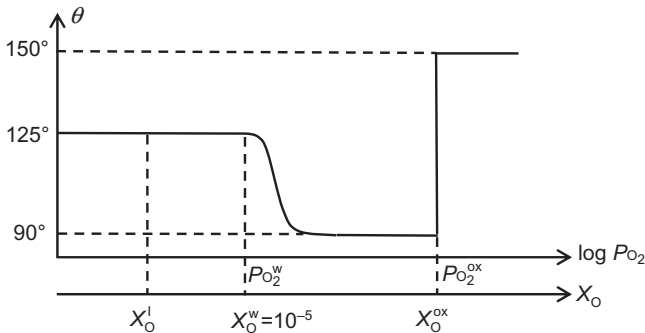


Figure 1.16 Schematic representation of the variation of θ with $\log P_{O_2}$ at constant temperature for a given metal/oxide couple. The wetting transition occurs at $P_{O_2}^W$ and X_O^W . When the metal changes, X_O^I and X_O^{OX} change too but X_O^W remains nearly constant [Eustathopoulos 2001]. However, the value of $P_{O_2}^W$ is different from metal to metal.

Classical examples are Al on Al₂O₃ [Laurent 1988] or molten silicides on SiC [Mailliart 2008] (see also Figure 6.28). Figure 1.17 shows the contact angle vs time curve for Ge on fused SiO₂ under high vacuum or Ar containing a few ppm of oxygen. In high vacuum, steady contact angles close to 115° are observed. When Ar is introduced the contact angle increases strongly towards 155°, indicating liquid oxidation. As a general rule, the effect of a skin on wetting predominates in the low temperature–high P_{O_2} ranges. As shown in Table 1.3, the $P_{O_2}^{OX}$ value in equilibrium with the oxide of the metal at a temperature close to its melting point is much lower than typical P_{O_2} values in regular neutral gas atmospheres (10^{-6} – 10^{-8} atm), resulting in skin formation. Some elements such as Al and Si can form volatile suboxides. Then, the reaction between the skin and the underlying metal (for instance the reaction $(Si) + <SiO_2>_{skin} \rightarrow 2[SiO]$) favors deoxidation which can occur at P_{O_2} values in the furnace much higher than $P_{O_2}^{OX}$ [Laurent 1988, Castello 1994]. Obtaining clean surfaces is much easier in high vacuum where the removal of SiO (or Al₂O) gaseous species far from the metal surface is much easier than in neutral gas

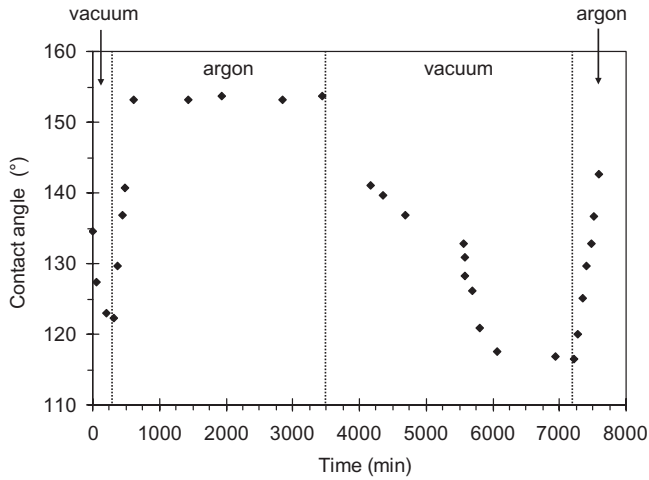


Figure 1.17 Contact angle of Ge on fused silica showing the effect of a change between dynamic vacuum and 1040mbar Ar on the wetting angle. Data from work reported in (Reprinted with permission from [Kaiser 2001], copyright (2001) Elsevier Ltd).

Table 1.3 Partial pressure of oxygen in equilibrium with the oxide of the metal at the temperature of fusion of the metal T_m^M and at 1000°C

Metal/metal oxide	T_m^M (°C)	$P_{O_2}^{ox}(T_m^M)$ (atm)	$P_{O_2}^{ox}(1000^\circ\text{C})$ (atm)
Al/Al ₂ O ₃	660	3×10^{-52}	10^{-35}
Pb/PbO	327	2×10^{-28}	8×10^{-9}
Sn/SnO ₂	232	10^{-50}	6×10^{-14}
Si/SiO ₂	1412	10^{-19}	10^{-28}
Ge/GeO ₂	950	2×10^{-15}	2×10^{-14}
Ga/Ga ₂ O ₃	30	2×10^{-113}	6×10^{-19}
In/In ₂ O ₃	157	9×10^{-63}	10^{-14}
Sb/Sb ₂ O ₃	631	10^{-18}	4×10^{-11}
Cd/CdO	321	8×10^{-43}	8×10^{-9}
Te/TeO ₂	450	2×10^{-14}	10^{-4}

atmospheres [Mailliart 2008]. In some cases, the metal oxide is liquid and can react with the oxide substrate, thus promoting wetting and adhesion. On cooling, sticking can be observed. An example is PbO formed during wetting of Pb on SiO₂ substrates [Sangiorgi 1995, Eustathopoulos 1999 p. 230].

The above considerations concern metals (M) for which the thermodynamic stability of the MO_n oxide, as reflected by its Gibbs energy of formation ΔG_0^f , is much lower than that of the oxide substrate (see also the values of $P_{O_2}^{ox}$ at 1000°C in Table 1.3, which are calculated from ΔG_0^f). This is no longer the case for molten Si on SiO₂. Indeed, the value of X_O^I for the Si/SiO₂ system at a temperature close to the melting point of Si is in the range 5×10^{-5} – 15×10^{-5} , i.e. above the X_O^w value defining the wetting transition

(Figure 1.16). This can explain the contact angles close to 90° observed for molten Si on SiO_2 (Table 1.2) and also on Al_2O_3 , MgO and ZrO_2 [Maeda 1986, Yuan 2004]. However, it is likely that Si (like Al) also modifies the surface chemistry and structure of the oxide substrate itself, as discussed in [Eustathopoulos 1998, Eustathopoulos 1999 p. 216].

Consider now an alloying element added in a nonreactive, nonwetting matrix M on a ionocovalent oxide. If the alloying element develops weak, van der Waals, interactions with the oxide substrate, as the matrix M, the effect of the alloying element on wetting is expected to be small and even negligible. This is consistent with the thermodynamic model of Li *et al.* [Li 1989]. This explains the small variation of contact angle for Ga–Sb on SiO_2 when varying the composition of the liquid between pure Ga ($\theta = 136^\circ$) and pure Sb ($\theta = 132^\circ$) [Cröll 2003]. A similar behaviour has been observed for In–Sb mixtures [Harter 1993].

A more significant effect can be observed by the addition of an element developing, by adsorption, chemical interaction with the oxide substrate, such as Si in Ge (see Table 1.2). This effect is important for the first few per cent of the addition, further addition having much less effect.

Note that in Table 1.2 differences of about 10° in θ values measured in the same system by different teams are not surprising, taking into account differences in P_{O_2} , substrate roughness, experimental procedure and method for obtaining θ values from drop images. Among the results presented in Table 1.2, the case of CdTe is rather puzzling. In the absence of oxygen in the quartz ampoule containing the sessile drop, Cd and Te cannot react with SiO_2 as their $P_{\text{O}_2}^{\text{x}}$ values are much higher than the value for Si (Table 1.3). Therefore, according to the previous developments, in the absence of oxygen the equilibrium contact angle would be much higher than 90° . Oxygen present in the ampoule can dissolve in CdTe, thus reducing the contact angle. However, to our knowledge, no data exist showing a significant solubility of O in CdTe. Moreover, an explanation based on dissolved oxygen can hardly explain the comparatively marked decrease of θ (15°) observed in [Shetty 1990a] for a limited increase of temperature (60 K). Indeed, for a given value of P_{O_2} , the molar fraction of oxygen dissolved in a liquid metal or alloy decreases when the temperature increases. Another possibility for the oxygen in the ampoule is to form a liquid oxide such as TeO_2 likely to react with SiO_2 , thus improving wetting and adhesion. Such an effect was observed by Yasuda *et al.* [Yasuda 1990], cited in [Cobb 1999], who found that TeO_2 in the starting charge of CdTe ingots reacted with the quartz ampoule, causing adhesion. The same situation was likely to occur with ZnO_2 and SeO_2 when solidifying $\text{Hg}_{1-x}\text{Zn}_x\text{Se}$ alloys in quartz ampoules [Cobb 1999].

Semiconductors on Carbon-Based Substrates. The wettability of carbon-based substrates by liquid metals and semiconductors depends on the liquid/carbon reactivity. Three cases can be distinguished [Eustathopoulos 1999 p. 317]: (i) very low solubility of carbon in the liquid (typically <100 ppm), (ii) high solubility, and (iii) formation of metal carbide at the interface. Only (i) and (iii) are considered here.

Nonreactive pure metals (such as In, Ga, Sb, Pb, Sn, Cu, Ag) do not wet carbon substrates ($\theta \gg 90^\circ$) whatever the type of carbon: vitreous carbon (C_v), graphite (C_g), or diamond (C_d). As for ionocovalent oxides, adhesion in these systems is ensured by weak, van der Waals, interactions. As a result, for a given system, θ changes only slightly with temperature (typically by $1\text{--}2^\circ$ for every 100 K). Moreover, the addition of a nonreactive

element in a nonreactive matrix produces a change in θ of only 5–15° [Eustathopoulos 1999 p. 324]. All the semiconductors listed in Table 1.4, except Si and Ge–Si alloys, belong to this type of nonreactive, nonwetting, system. Note that for a given element, the contact angles on smooth surfaces of C_v are higher by 15–20° than those on basal faces of monocrystalline graphite because of the lower atomic density of vitreous carbon [Dezellus 1999]. For polycrystalline graphite, very large contact angles are often observed (150–160°). However, these values are due to its high roughness (it is difficult to prepare polycrystalline graphite surfaces with an average roughness less than 100 nm) and also to porosity (in nonwetting systems pores act as a second phase with $\theta_\beta = 180^\circ$ in Cassie's Equation (1.15)).

Reactive wetting will be considered only for pure Si and Ge–Si alloys. Si reacts with C forming at the interface a continuous layer of SiC, a few microns in thickness. Figure 1.18 shows the change with the logarithm of time of the contact angle of Si on a smooth surface of C_v . When time tends towards zero, the contact angle tends towards 150°, which is the contact angle of Si on unreacted carbon (see also Figure 1.14). The final contact angle of 36° is very close to the contact angle of Si on SiC. As a general rule, reported values for polycrystalline graphite are in the range 5–15°, i.e. lower than those on C_v .

Table 1.4 *Contact angle of semiconductors on carbon-based substrates*

Semiconductor	Substrate	Temperature (°C)	Atmosphere	θ_f (°)	Reference
Ge	C_v	1100	High vacuum	157	[Kaiser 2001]
				166	
Ge	C_g	1000	High vacuum	139	[Naidich 1968]
Ge	C_d CVD	1100	High vacuum	146	[Kaiser 2001]
Ge	C_d	1000	High vacuum	136	[Naidich 1981]
GaSb	C_v	920	High vacuum	128	[Harter 1993]
				no sticking	
InSb	C_v	800	High vacuum	124	[Harter 1993]
				no sticking	
CdTe	C_v	1100	High vacuum	116	[Katty 1992]
			+ Cd vapour		
$Cd_{0.96}Zn_{0.04}Te$	C_v	1100	High vacuum	126	[Katty 1992]
			+ Cd vapour		
GaAs	C-coated SiO_2	1238	High vacuum	120	[Shetty 1990b]
			+ As vapour		
Ga–In–As	C_g	632	H_2	148	[König 1984]
InP	C_g	632	H_2	144	[König 1984]
Si	C_g	1450	High vacuum	15	[Naidich 1981]
Si	C_v	1430	High vacuum	36	[Dezellus 2005]
Ge–4.6 at.% Si	C_v -coated C_g	1100	High vacuum	103	[Cröll 2002]
Ge–20 at.% Si	C_v	1231	High vacuum	55	[Dezellus 2000]

C_d , diamond; C_g , graphite; C_v , vitreous carbon.

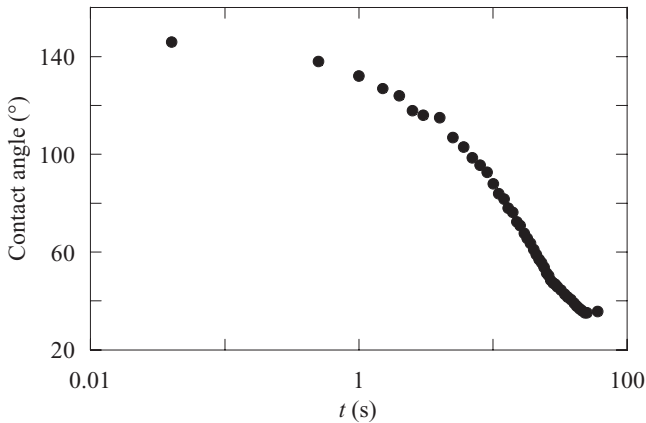


Figure 1.18 Variation of contact angle with time for Si on C_v at 1430°C (Reprinted with kind permission from [Dezellus 2005], copyright (2005) Springer).

Indeed, for wetting systems ($\theta \ll 90^\circ$), roughness favours wetting, as indicated by the Wenzel Equation (1.11). Moreover, Si can infiltrate the open porosity of graphite ahead of the drop triple line. In this case, filled pores act as a second phase with $\theta_\beta = 0^\circ$ in Cassie's Equation (1.15). Finally, infiltration decreases the drop volume leading to a receding contact angle instead of an advancing one.

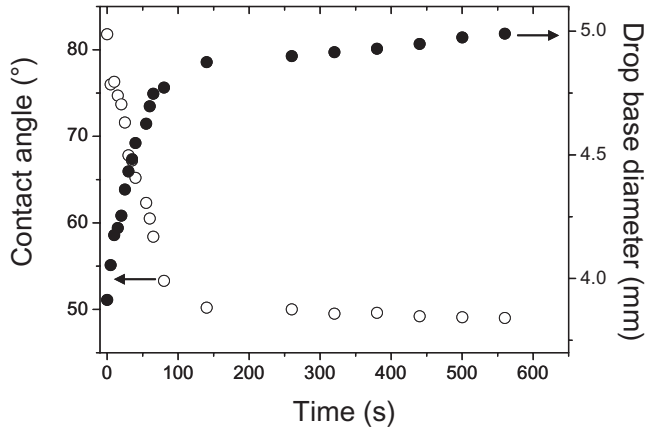
Ge does not wet C_v (Table 1.4) but the addition of Si promotes wetting by forming a wettable SiC layer at the solid/liquid interface. For the Ge-20 at.% Si alloy, a steady contact angle of 55° is reached in 1300s at 1231°C (Figure 1.13). However, for the Ge-4.6 at.% Si alloy, the driving force of the interfacial reaction at 1100°C is much lower, resulting in very slow spreading kinetics: the contact angle decreases from an initial value of 150° to a value close to 110° within a day [Cröll 2002]. However, it is possible that the value of 103° reported in Table 1.4 is not a steady angle.

Semiconductors on Nitrides. Al and Si nitrides are nonoxide but oxidizable ceramics. Indeed, even a very short time (1–2 min) in contact with air at room temperature leads to the formation of nanometre-thick oxide or oxi-nitride layers. These layers are stable even in high vacuum environments. For instance, in the case of Si_3N_4 , several hours at 1140°C in an ultrahigh vacuum are needed to remove oxygen. Therefore, at temperatures lower than 1100°C, in neutral gas or standard vacuum environments employed in crystal growth, wettability of Al and Si nitrides is imposed by oxygen-rich surface layers. As a consequence, the contact angle of nonreactive metals such as In, Sn, Ga, Pb, Sb, Ag on these nitrides is in the range 110–140°, as on ionocovalent oxides. Among semiconductors, Ge and GaSb form also nonwetting contact angles (Table 1.5).

The initial contact angle of Si on Si_3N_4 is close to 80° , as on SiO_2 substrates (see Table 1.2). However, the contact angle decreases rapidly with time and tends towards 49° , which is close to the intrinsic contact angle of Si on Si_3N_4 (Figure 1.19). The spreading kinetics in this system are controlled by substrate deoxidation occurring by reaction between liquid Si and the oxide layer at the triple line with formation of volatile SiO [Drevet 2009]. For Ge–Si alloys on Si_3N_4 , Cröll *et al.* [Cröll 2002] also observed a

Table 1.5 Contact angle of semiconductors on Al and Si nitrides

Semiconductor	Nitride	Temperature (°C)	Atmosphere	θ_f (°)	Reference
Ge	AlN sintered	950	High vacuum	122	[Naidich 1995]
Ge	AlN sintered	1100	Vacuum/Ar	153	[Kaiser 2001]
Si	AlN CVD	1430	H ₂ $P_{O_2} = 8.7 \times 10^{-16}$ Pa	45	[Barsoum 1981]
Si	AlN sintered	1412	High vacuum	48	[Naidich 1995]
Ge-6.3 at.% Si	AlN sintered	1100	Vacuum/Ar	124	[Cröll 2002]
GaSb	AlN pyrolytic	820	High vacuum	103	[Harter 1993]
Ge	Si ₃ N ₄ sintered	1100	Vacuum/Ar	136	[Kaiser 2001]
Si	Si ₃ N ₄ CVD	1430	H ₂ $P_{O_2} = 10^{-15}$ Pa	48–52	[Barsoum 1981]
Si	Si ₃ N ₄ sintered	1430	Ar	49	[Drevet 2009]
Ge-6.2 at.% Si	Si ₃ N ₄ sintered	1100	Vacuum/Ar	96	[Cröll 2002]

**Figure 1.19** Contact angle and drop base diameter as a function of time for a Si drop on sintered Si₃N₄ at 1430 °C (Reprinted with permission from [Drevet 2009], copyright (2009) Elsevier Ltd).

decrease of the contact angle from 150° towards 96° (Table 1.5) probably occurring by a similar process. However, due to the low thermodynamic activity of Si and the comparatively low temperature, the spreading time is very high (several hundreds of minutes). Similar phenomena occur with Ge–Si alloys on AlN [Cröll 2002].

BN is also an oxidizable ceramic but boron oxide, B₂O₃, which is liquid above 450 °C, is a volatile oxide such that clean BN surfaces are expected to form at higher temperatures, especially in high vacuum. Nonreactive metals such as Ga, Sn, Ag, Au do not wet BN at temperatures of 1000–1100 °C, the contact angle being in the range 130–150° [Naidich 1981]. No significant differences in wettability have been found between hexagonal and cubic BN [Naidich 1981]. Even higher contact angle values, close to 160–170°, have

Table 1.6 Contact angle of semiconductors on BN

Semiconductor	Substrate	Temperature (°C)	Atmosphere	θ_f (°)	Reference
Ge	BN pyrolytic	1100	Ar-2% H ₂	173	[Kaiser 2001]
Ge	BN cubic	1100	High vacuum	138	[Naidich 1981]
	BN hexagonal	1100	High vacuum	139	
Si	BN pyrolytic	1430	Ar	117	[Drevet 2009]
Si	BN cubic	1500	High vacuum	95	[Naidich 1981]
	BN hexagonal	1500	High vacuum	110	
Si	BN pyrolytic	1500	High vacuum	105	[Champion 1973]
Ge-7.1 at.% Si	BN pyrolytic	1100	vacuum/Ar	168	[Cröll 2002]
GaSb	BN pyrolytic	920	High vacuum	129	[Harter 1993]
InSb	BN pyrolytic	800	High vacuum	134	[Harter 1993]
InP	BN pyrolytic	1065	High vacuum + P vapour	140–150	[Shimizu 2002]
CdTe	BN pyrolytic	1092	High vacuum + Cd vapour	132	[Shetty 1990a]
GaAs	BN pyrolytic	1238	High vacuum + As vapour	155	[Shetty 1990b]

been reported in the literature, mainly due to roughness effect. The wetting of Ge, GaSb, InSb, InP, CdTe and GaAs on BN is the same as that of nonreactive metals (Table 1.6).

Molten Si does not wet the different forms of BN, but the contact angles are significantly lower than for nonreactive semiconductors (Table 1.6). Moreover, despite this nonwetting behaviour, sticking has been observed in the Si/BN system. These phenomena were explained in [Drevet 2009] by the reaction between Si and BN leading to the formation of Si₃N₄ at the interface $3(\text{Si}) + 4\langle\text{BN}\rangle \rightarrow \langle\text{Si}_3\text{N}_4\rangle + 4(\text{B})$. However, the reactivity in the Si/BN system is so weak that chemical equilibrium (i.e. saturation of liquid Si with B) is established well before the equilibrium contact angle on the reaction product (i.e. Si₃N₄) is attained.

Ge–Si alloys with a low Si content are nonreactive with BN, such that the presence of Si in the melt does not affect the contact angle of Ge on BN (Table 1.6).

1.2.4.2 Oxide/Metal and Oxide/Carbon Systems

Although several articles have been devoted to crystal growth of oxides in contact with refractory metals (Pt, Ir, Mo, W), only a few give measurements of contact angles. In contrast, a significant number of wettability studies has been performed with oxide slags and glasses. One can reasonably expect that the conclusions drawn from these studies can also be applied to oxide/metal systems that are relevant in crystal growth.

In nonreactive molten oxide/solid metal systems, as in nonreactive liquid metal/ionocovalent oxide ones, adhesion results from weak, van der Waals, interactions leading to values of work of adhesion W_a of a few hundreds of mJ m⁻². However, while liquid metals do not wet ionocovalent oxides, molten oxides wet metallic substrates ($\theta < 90^\circ$, Table 1.7). The reason for this difference is the very different values of surface tension between

Table 1.7 Contact angles of soda-lime glass (13.4 wt% Na₂O, 10.9 wt% CaO, 1.6 wt% Al₂O₃, 1.4 wt% MgO, SiO₂ bal.) on different substrates at temperatures close to 1000 °C

Substrate	Atmosphere	θ_f (°)
X25V steel	He	65 ± 3
Pt	He	75 ± 3
Au	N ₂	60 ± 3

Reprinted with permission from [Pech 2004], copyright (2004) Elsevier Ltd.

molten metals and molten oxides. For instance, γ_v of molten SiO₂ at 1720 °C is 300 mJ m⁻² while at the same temperature γ_v of molten Ni is six times higher. Thus, for liquid metals, γ_v is higher than W_a , resulting in nonwetting according to the Young–Dupré Equation (1.9). Conversely, for molten oxides, $\gamma_v < W_a$, leading to $\theta < 90^\circ$. The physical reason for which the surface tension of molten oxides is low, comparatively to their cohesion energy, is discussed in [Eustathopoulos 1999 p. 164].

A feature of van der Waals interactions is lack of selectivity. For instance, the contact angle of soda-lime glass on a stainless steel rich in Cr, a metal with a high affinity for oxygen, is close to the contact angle observed for the same glass on the noble metals Pt and Au (Table 1.7). However, the mechanical behaviour of the solid oxide/metal substrate system on cooling is very different. Indeed, soda-lime glass adheres on Pt but not on steel substrates. The adhesion energy in these systems is very close, as well as the elastic modulus of contacting phases. However, $\Delta\alpha$ is very different, close to zero in the case of Pt ($< 0.2 \mu\text{m m}^{-1} \text{K}^{-1}$) and very high in the case of stainless steel ($\cong 10 \mu\text{m m}^{-1} \text{K}^{-1}$) [Pech 2004].

For a given mixture of oxides on Pt substrate, when the wetting experiments are performed in air, the contact angles are found systematically lower by 10–30° than those measured in a neutral gas atmosphere (50–80°). This effect was attributed to the formation on the metal surface of a layer of chemisorbed oxygen [Eustathopoulos 1999 p. 345]. Indeed, with metal atoms adsorbed oxygen forms a partially ionocovalent bond that increases the adhesion energy of the solid metal with the molten oxide. Such an adsorption effect on adhesion was evidenced by Ownby *et al.* [Ownby 1995] who found a significant decrease in contact angle, occurring above a given value of P_{O_2} in the gas, in a range where no oxidation of the W substrate takes place (Figure 1.20). Oxidation of the solid metal can enhance wetting, but this usually leads to dissolution of the oxide layer in the molten oxide, which may locally increase the viscosity and thus reduce the spreading rate. Duffar *et al.* [Duffar 2009] report melting studies of BGO in Ir where an increase of P_{O_2} above 0.1 mbar promotes Ir oxidation, leading to a decrease in the contact angle (from 70° to 0°) and sticking.

Nonreactive oxides do not wet carbon. Indeed, contact angles as high as 130–140° have been observed for various oxides on vitreous carbon or graphite [Ellefson 1938, Towers 1954, Pech 2005]. Reactivity promotes wetting. For instance, molten B₂O₃ reacts with C_v, leading to contact angles as low as 30–40° [Wery 2008]. In this system, it seems that wettability is improved by the formation at the interface of B₄C, a compound wettable by the oxide.

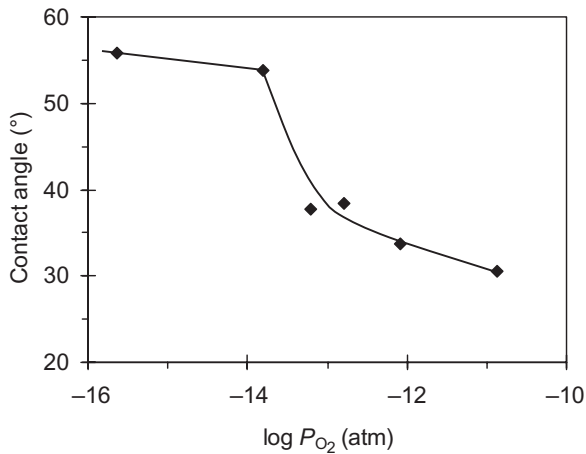


Figure 1.20 Contact angle values as a function of $\log P_{O_2}$ for $SiO_2-20Al_2O_3-10CaO-10MgO$ (wt.%) on W at 1400°C. Data from work reported in [Ownby 1995].

Table 1.8 Contact angles of molten salts measured on graphite immediately after melting

Salt	Temperature (°C)	θ (°)	γ_v (mJm ⁻²)
NaCl	810	113	114
KCl	780	78	99
RbCl	740	58	95
CsCl	645	31	92

Reprinted with permission from [Baumli 2008], copyright (2008) Elsevier Ltd.

1.2.4.3 Halide/Ceramic Systems

Molten halides have low γ_v values (in the range 50–250 mJ m⁻²) comparatively to other molten substances, such as metals and even oxides. The thermodynamic adhesion of molten halides on carbon is weak, as ensured solely by physical interactions [Baumli 2008]. From modelling molten halide/graphite interactions, it was shown that for the same type of halides (for instance chlorides), when the surface tension decreases, the work of adhesion increases rapidly. According to the Young–Dupré Equation (1.9), this implies a strong decrease in the contact angle (Table 1.8). Similarly, while large nonwetting contact angles (130–150°) were found for LiF ($\gamma_v = 236$ mJ m⁻²) and NaF ($\gamma_v = 186$ mJ m⁻²), the contact angle of KF ($\gamma_v = 144$ mJ m⁻²) was found to be 80° and that of CsF ($\gamma_v = 106$ mJ m⁻²) was 41° [Morel 1970].

Like molten oxides, molten halides seem to wet metallic substrates. An example is molten LiF on various metals. In all cases, $\theta < 90^\circ$ but significant differences were found, for instance between Ta ($\theta = 4^\circ$) and Ni ($\theta = 62^\circ$) or Pt ($\theta = 68^\circ$) [Jaworske 1989].

1.3 Growth Angles

This section begins with a review of the basic theory underlying the concept of the growth angle, important in meniscus-defined melt growth systems, in the case of both isotropic and anisotropic interfacial energies. Next, various methods for measuring growth angles are discussed and data resulting from such measurements are presented. This is followed by a brief report on the application of the growth angle condition in simulations of crystal growth, as well as by the description and application, in a number of systems, of a method for determining and rigorously verifying the growth angle (assumed constant). The constant angle assumption, as well as the impact of heat transport and interface-attachment kinetics on the verification procedure (effectively involving a small-scale crystal growth simulation), are also discussed.

1.3.1 Theory

The concept of the growth angle stems from the early work on equilibrium at a junction between several phases. Consider Figure 1.21, which depicts the case relevant to this section: three phases (solid, liquid, and vapour) in equilibrium with one another along their line of mutual contact, the TPL, which is normal to the plane of the figure. Herring used an energy minimization approach [Herring 1951] to derive a vector condition, which in our case is given by the following sum of coplanar vectors:

$$\gamma_{sl}\mathbf{e}_{sl} + \gamma_{sv}\mathbf{e}_{sv} + \gamma_{lv}\mathbf{e}_{lv} + \gamma'_{sl}\mathbf{e}_{sl}^{\dagger} + \gamma'_{sv}\mathbf{e}_{sv}^{\dagger} + \gamma'_{lv}\mathbf{e}_{lv}^{\dagger} = \mathbf{0}. \quad (1.21)$$

The first three terms of Equation (1.21), containing the three interfacial energies together with the unit vectors tangent to the three interfaces, are related to the system's tendency

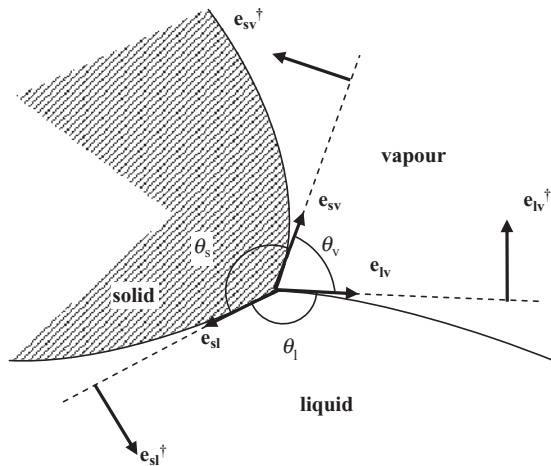


Figure 1.21 The triple phase line (TPL) with associated vectors and angles between interfaces.

to minimize the area of the more energetically expensive interfaces via contraction. The last three terms involve the derivative of the three energies with respect to the angular coordinate (measured in a counterclockwise sense around the TPL), together with unit vectors normal to the interfaces. These so called ‘torque terms’ reflect the system’s resistance to the change of interfacial orientation in a manner leading to the increase of energy due to its angular dependence.

1.3.1.1 Isotropic Interfacial Energies

The liquid/vapour interfacial energy is isotropic (i.e. $\gamma'_{lv} = 0$) and therefore the last term on the left-hand side of Equation (1.21) can be dropped. Now consider the case where both the solid/fluid interfacial energies do not depend on orientation ($\gamma'_{sl} = \gamma'_{sv} = 0$), yielding the isotropic form of the Herring equation. The resultant vector equation is often presented as two independent scalar equations relating interfacial energies and angles between interfaces. One form, originally proposed by Smith [Smith 1948], is given by Equation (1.10). A different representation of the same conditions is given [Voronkov 1963, Bardsley 1974] by:

$$\cos \alpha = \frac{\gamma_{sv}^2 + \gamma_{lv}^2 - \gamma_{sl}^2}{2\gamma_{sv}\gamma_{lv}}, \quad \cos \beta = \frac{\gamma_{sv}^2 + \gamma_{sl}^2 - \gamma_{lv}^2}{2\gamma_{sv}\gamma_{sl}} \quad (1.22)$$

where the first angle, defined as $\alpha = \pi - \theta_v$, is the growth angle and the second angle is defined as $\beta = \pi - \theta_s$.

The two isotropic relations for α and β given in Equation (1.22), together with the trivial equality $\theta_v + \theta_l + \theta_s = 2\pi$, provide the *intrinsic* values of the three angles between the interfaces as a function of the three interfacial energies. However, when viewing the TPL from a macroscopic viewpoint, it is not obvious that these angles will be preserved. This depends on the distance from the TPL over which the slope of the interface (i.e. its orientation) can be assumed constant. In the case of the liquid/vapour interface the relevant distance (see e.g. [de Gennes 2004]) is of the order of the capillary length ($l_c = \sqrt{\gamma_{lv}/\rho_l g}$), where ρ_l and g are, respectively, the liquid phase density and the acceleration due to gravity. Since, in typical crystal growth systems, the resultant value of l_c is of the order of millimetres, it is reasonable to assume that the slope of this interface at the TPL can be observed from a macroscopic viewpoint.

The solid/liquid interface typically conforms to the melting point isotherm (whose shape and position is governed by heat transport) except near the TPL where it must curve away from the isotherm to satisfy Equation (1.22) at the TPL. The curvature is related to the local undercooling at the TPL via the Gibbs–Thomson equation (see e.g. [Flemings 1974]), where the distance from the TPL over which the deviation from the isotherm occurs typically ranges from a few microns to several hundredths of a micron (see e.g. [Voronkov 1978, Voronkov 1981]).

Most interesting is the possibility of local (close to the TPL) variations in the slope of the solid/vapour interface. Following Voronkov [Voronkov 1978], consider the curvature of the solid/vapour interface, whose value at the TPL can be associated with the undercooling at this point. The surface gradient of this curvature can be related to a process of surface transport and deposition of mass from the liquid phase at the TPL to a point far

from the TPL where the curvature is negligible and the solid/vapour interface can be considered ‘finally formed’. The resultant deviation between the intrinsic growth angle α and the (effective) growth angle α^* , measured with respect to the slope at this point, is depicted in Figure 1.22. Quantification of this deviation [Voronkov 1978], assuming steady-state solidification and an isotropic solid/vapour interfacial energy near the TPL, yields:

$$\alpha^* = \alpha - \chi_0 = \alpha - Cv^{-1/3} \Delta T. \quad (1.23)$$

The angle χ_0 appearing in this equation is marked in Figure 1.22, ΔT (given by $\Delta T = T_m - T$) is the undercooling at the TPL, T is the temperature at the TPL, T_m is the material’s melting point, v is the crystal growth rate in the direction tangent to the solid/vapour interface far from the TPL, and C is a coefficient given by:

$$C = \frac{\Delta H}{T_m} \left[\frac{\lambda}{(\gamma_{sv} \hat{N})^2} \right]^{1/3}. \quad (1.24)$$

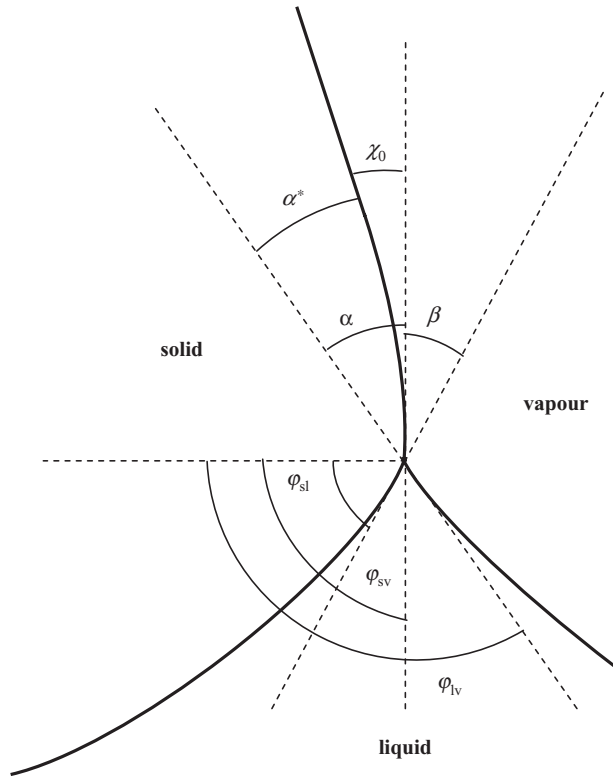


Figure 1.22 *Important angles at the TPL.*

In Equation (1.24) ΔH is the volumetric latent heat of fusion of the crystal, \hat{N} is the atomic density of the crystal and λ is the surface mass transport coefficient. Assuming a surface diffusion mechanism of mass transport yields:

$$\lambda = \frac{D_s \hat{N}_s}{k_B T}, \quad (1.25)$$

where D_s , \hat{N}_s and k_B are, respectively, the surface diffusion coefficient, the atomic surface density of the crystal and the Boltzmann constant. In the next section, concerned with anisotropic interfacial energies, an example related to the growth of silicon is used to obtain a feel for values of χ_0 in typical semiconductor growth systems (with and without isotropic interfacial energies).

1.3.1.2 Anisotropic Interfacial Energies

Consider the more general case of anisotropic fluid/crystal interfacial energies. Following Bardsley *et al.* [Bardsley 1974], a scalar multiplication of the relevant form of the Herring equation (Equation (1.21) with $\gamma'_{lv} = 0$) with the unit vectors \mathbf{e}_{sv} and \mathbf{e}_{lv} yields two relations uniquely defining α and β :

$$\begin{aligned} \gamma_{sv} - \gamma_{lv} \cos \alpha - \gamma_{sl} \cos \beta - (\gamma'_{sl}|_{\varphi_{sl}}) \sin \beta &= 0 \\ \gamma_{lv} - \gamma_{sv} \cos \alpha + \gamma_{sl} \cos(\alpha + \beta) - (\gamma'_{sv}|_{\pi + \varphi_{sv}}) \sin \alpha + (\gamma'_{sl}|_{\varphi_{sl}}) \sin(\alpha + \beta) &= 0, \end{aligned} \quad (1.26)$$

where, following Figure 1.22, the angular derivatives of the interfacial energies are taken with respect to φ , which is measured counterclockwise from the horizontal.

Using Equation (1.26) allows for the determination of α and β provided all three interfacial energies are known where, in the case of the two solid/fluid interfaces, the angular dependence of these energies is also required. Alternatively, Equation (1.26) can be used, together with experimental and calculated data for average values of the interfacial energies and angles α and β , to obtain rough estimates for the contributions of the torque terms in these two relations (see e.g. [Bardsley 1974] for such an estimate in the case of the growth angle of Ge).

The relations in Equation (1.26) specify the intrinsic angles α and β as long as the two solid/fluid interfacial energies (γ_{sl} , γ_{sv}) are continuously differentiable at the relevant angular orientation of these interfaces (φ_{sl} and $\pi + \varphi_{sv}$; see Figure 1.22). As in the case of isotropic energies, there is the possibility that macroscopically observed angles will differ from their intrinsic values. The above discussion of this issue is still relevant though certain restrictions apply (related to anisotropy of the solid/vapour interface). Of special interest is the case where a facet exists on the solid/liquid interface near the TPL. The resultant typically nonnegligible value of ΔT at the TPL associated with such a facet is often associated with an appreciable difference between α and α^* according to Equation (1.23).

To obtain a feeling for values of χ_0 in typical semiconductor growth systems, consider the case of a dislocation-free silicon crystal grown by the Czochralski method in the $\langle 111 \rangle$ direction, where a ring-shaped facet appears on the solid/liquid interface near the TPL

(see e.g. [Voronkov 1975]). The undercooling at the TPL is $\Delta T = 3.7^\circ\text{C}$ and the experimentally based estimated value of χ_0 is of the order of 20° (see [Voronkov 1978] and references therein). In the event that a facet is not present near the TPL, the undercooling is two orders of magnitude smaller (see e.g. [Voronkov 1974]). Assuming a similar growth velocity and treating C (in Equation (1.23)) as a constant suggests that the value of χ_0 is negligible and the effective observable growth angle is, in this case, equal to α . This important conclusion implies that a typical semiconductor crystal growth system, whose growth front is facet-free in the vicinity of the TPL and whose solid/vapour interfacial energy can be assumed isotropic, is likely to exhibit a macroscopically observable growth angle which is the thermodynamic constant α given by Equation (1.26); in the event that both solid/fluid interfacial energies are isotropic the growth angle will be given by Equation (1.22).

Systems exhibiting facets in contact with the TPL cannot be analysed using Equation (1.26) since the interfacial energy associated with faceted surfaces is not continuously differentiable with respect to orientation at the relevant value of φ . In this case it is useful to consider graphical solutions to Equation (1.21). Two similar approaches have been proposed, the first in [Hoffman 1972] and the second in [Voronkov 1980; Voronkov 1981]. In the following the approach described in [Voronkov 1981] is presented.

First, two two-dimensional polar (Wulff) plots are constructed, one for γ_{sl} and the other for γ_{sv} . For each surface orientation \mathbf{n}_{ij} a segment of length $\gamma_{ij}(\mathbf{n}_{ij})$ is drawn from the origin in the direction of \mathbf{n}_{ij} ($ij = \text{sl}$ or sv); note that (see Figure 1.21) $\mathbf{n}_{\text{sl}} = \mathbf{e}_{\text{sl}}^\dagger$ and $\mathbf{n}_{\text{sv}} = -\mathbf{e}_{\text{sv}}^\dagger$. Next, a straight line perpendicular to this segment is drawn at its end. The family of these straight lines defines an inner closed form whose boundary is denoted by Γ_{ij} ($ij = \text{sl}$ or sv). Examples of the two resultant forms are depicted in Figure 1.23. Note that in this specific case a system has been chosen which exhibits one singular orientation (identical for both solid/fluid interfaces), associated with a cusp in the two Wulff plots.

Consider a vector \mathbf{g}_{ij} drawn from the origin to some point on Γ_{ij} ($ij = \text{sl}$ or sv). It can be shown (see e.g. [Voronkov 1980]) that:

$$\mathbf{g}_{ij} = \gamma_{ij}\mathbf{n}_{ij} + \gamma'_{ij}\mathbf{n}_{ij}^\dagger \quad (ij = \text{sl}, \text{sv}, \text{lv}), \quad (1.27)$$

where (see Figure 1.21) $\mathbf{n}_{\text{sl}}^\dagger = -\mathbf{e}_{\text{sl}}$, $\mathbf{n}_{\text{sv}}^\dagger = \mathbf{e}_{\text{sv}}$, $\mathbf{n}_{\text{lv}}^\dagger = -\mathbf{e}_{\text{lv}}$ and $\mathbf{n}_{\text{lv}} = \mathbf{e}_{\text{lv}}^\dagger$; notice that the definition of the vector \mathbf{g}_{ij} is given for all three interfaces ($ij = \text{sl}, \text{sv}, \text{lv}$). Let us now rotate the Herring equation, Equation (1.21), by $\pi/2$ in the counterclockwise direction where this can be achieved by performing a scalar multiplication of this equation (with $\gamma'_{\text{lv}} = 0$) from the left by an appropriately chosen dyadic. Inserting into the resultant vector equation, for all three interfaces, the relation given by Equation (1.27) yields:

$$\mathbf{g}_{\text{sl}} - \mathbf{g}_{\text{sv}} + \mathbf{g}_{\text{lv}} = \mathbf{0}. \quad (1.28)$$

Following Voronkov [Voronkov 1981], for a given solid/vapour interfacial orientation at the TPL (\mathbf{n}_{sv}), assuming the three interfacial energies are known (as a function of orientation), it is possible to use Equation (1.28) together with the two Γ plots in Figure 1.23 to obtain the other two interfacial orientations \mathbf{n}_{sl} and \mathbf{n}_{lv} . First, the point on Γ_{sv} whose ori-

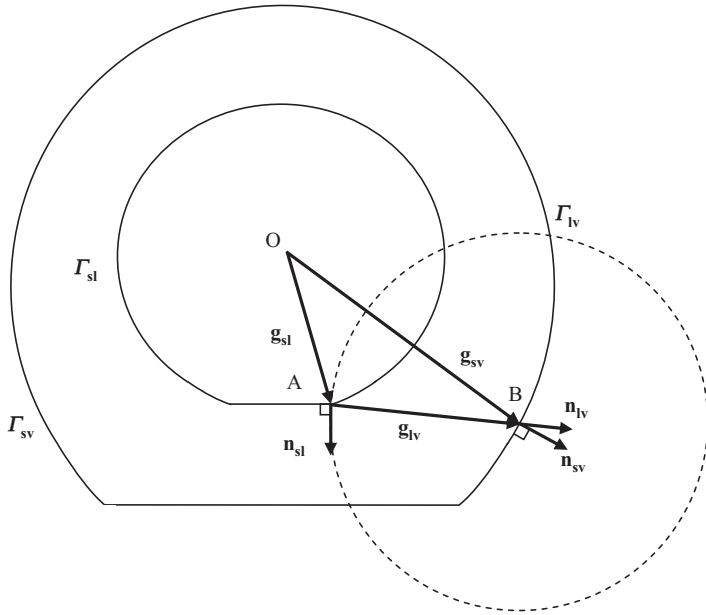


Figure 1.23 Geometric representation associated with the Herring equation (Equation (1.21)).

entation is \mathbf{n}_{sv} (point B) is located, where OB is the corresponding \mathbf{g}_{sv} vector. Drawing from point B a circle whose radius is equal to g_{lv} (i.e. γ_{lv}), determines point A which is the intersection of this circle with Γ_{sl} . The obtained vectors OA and AB are, respectively, equal to \mathbf{g}_{sl} and \mathbf{g}_{lv} , where the resultant closed triangle constructed by the three vectors is a graphical representation of Equation (1.28) and now all three orientations (\mathbf{n}_{sl} , \mathbf{n}_{lv} , \mathbf{n}_{sv} or φ_{sl} , φ_{lv} , φ_{sv}) are known. This result immediately yields the two intrinsic angles $\alpha = \varphi_{lv} - \varphi_{sv}$ and $\beta = \varphi_{sv} - \varphi_{sl}$. Finally, note (in Figure 1.23) the additional intersection point of the circle with Γ_{sl} . Although this point admits an additional solution to Equation (1.28), it must be rejected because the resultant interfacial orientations are not consistent with the physical picture involving, when moving in a counterclockwise direction around the TPL, a crossover from solid to liquid to vapour and back again to solid (see Figures 1.21 and 1.22).

The specific triangle of vectors in Figure 1.23 reflects the orientations of the three interfaces at a given point in time where, in the case of steady-state growth, all orientations are time-independent and the growth angle α is a constant. It is possible to think of several positions for point B, each with different corresponding orientations of the three interfaces. Plotting the resultant solid/fluid interfacial orientation angles (φ_{sl} , φ_{sv}) as a function of the angular orientation of the liquid/vapour interface (φ_{lv}) yields a useful figure of the type proposed in [Voronkov 1980]. A schematic of such a plot, qualitatively consistent with Figure 1.23 is shown in Figure 1.24; the point corresponding to the specific OAB triangle shown in Figure 1.23 is marked in Figure 1.24. Note that Figures 1.23 and 1.24 are not completely consistent with Figures 1.21 and 1.22, which do not show a facet

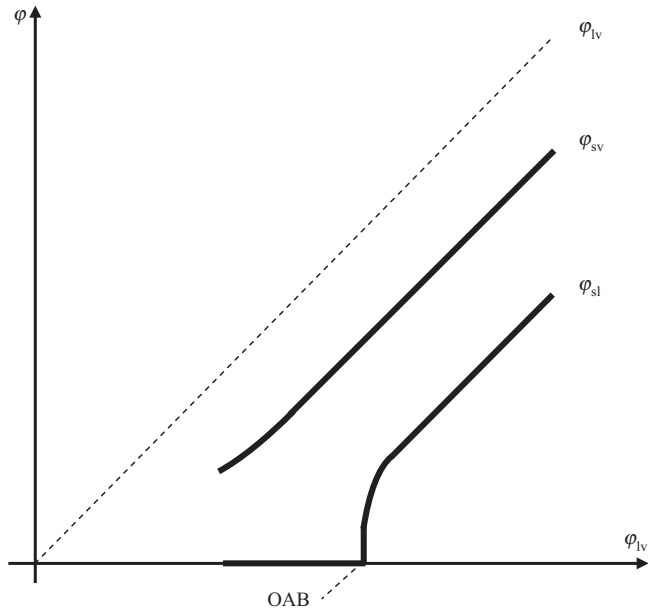


Figure 1.24 Relative orientations of the three interfaces. The dashed line corresponds to the 45° line (φ_{lv} vs φ_{lv}) and the point corresponding to the OAB construction in Figure 1.23 is marked.

on the solid/vapour interface at the TPL. In addition, it is important to note that the curves in Figure 1.24 are associated with a limited range of interfacial orientations and do not cover all possibilities that can be derived from Figure 1.23 (e.g. facets on the solid/vapour interface).

It is possible to relate γ'_{sl} to the relevant step energy (normalized by the step height) of a vicinal surface associated with the singular direction characterized by the specific \mathbf{n}_{sl} vector shown in Figure 1.23. As described in [Voronkov 1981], and consistent with Figure 1.23, γ'_{sl} on the singular surface jumps from the negative value associated with a negative vicinal surface slope to a positive value associated with a positive vicinal surface slope. As can be understood from Figures 1.23 and 1.24, a faceted solid/liquid surface in contact with the TPL may theoretically be associated with a variety of growth angles whose range can be related to the negative and positive vicinal slope step energy values. Interestingly, in [Yuferev 2005] it is shown how this phenomenon (in the context of a facet on the solid/vapour interface) may result in two distinctly different growth angles on the two sides of a sapphire ribbon grown by the EFG technique. Finally, in the case of isotropic energies, the two Γ plots are circular, the size and relative orientation (one with respect to the other) of the three vectors remain constant and, consistent with Equation (1.22), α and β also remain constant regardless of the position of point B. This situation can be observed in Figure 1.24 for large values of φ_{lv} at which the curves are parallel to one another (recall that $\alpha = \varphi_{lv} - \varphi_{sv}$ and $\beta = \varphi_{sv} - \varphi_{sl}$).

The above relatively simple picture of the graphical approach to the determination of the growth angle is misleading. First of all, real quantitative data on both Γ plots is not usually available. In addition, significant differences between the values of α and α^* can be expected in certain cases, providing further complications to the analysis. Additional nontrivial issues such as the possibility for metastable solutions are discussed in [Voronkov 1981]. Such complications lead to the practical approach according to which growth angles are typically measured from experiments. The analysis of the results of these can, however, benefit from an understanding of the above theoretical considerations.

1.3.2 Measurements of Growth Angles: Methods and Values

Over the past four decades there have been several efforts to measure growth angles in a number of melt growth systems. The measurement techniques can usually be classified as belonging to one of two main approaches, observation of the TPL region during growth (method 1) or an *a posteriori* analysis of solidified material (method 2). Method 1 involves either direct observation and measurement of the angle between tangents to the meniscus (liquid/vapour interface) and the solid/vapour interface at the TPL, or a mathematical analysis of the observed meniscus (and in some cases the solid/vapour interface) leading to the determination of the growth angle. Related measurements of contact angles of melt drops placed on substrates (e.g. relevant to liquid phase epitaxy [König 1983, König 1984]) are not discussed here.

In the following, several studies involving the application of methods 1 and 2 to the measurement of growth angles in a variety of systems are briefly discussed. Measured values, sorted according to the type of crystalline material studied, are listed in Table 1.9. Note also that partial lists of growth angles are reviewed in the literature ([Bohm 1994, Hurle 1994, Hurle 1995, Duffar 1997, Kuandykov 2001]).

The early measurements date back to the 1960s. Antonov [Antonov 1965] photographed the meniscus (including the TPL) of Ge growing by the Czochralski technique. He directly measured the angle between the tangent to the meniscus and the horizontal and, in addition, showed that two different values of this angle give a good fit to an approximate solution of the Young–Laplace equation for two different sets of experimental measurements of crystal diameter and meniscus height. The angles determined are equal to $\pi/2 - \alpha$ (where α is the growth angle) only if the measurements can be assumed to have involved a time-independent crystal diameter. Shashkov and Mel'inkov [Shashkov 1965] filmed the Czochralski growth process, applied to Ge and Si, to obtain direct observations of the growth angles of these materials. Further measurements using method 1 are reported by Wenzl *et al.* [Wenzl 1976, Wenzl 1978] who used a Czochralski growth process to determine the growth angles of Cu [Wenzl 1976] and Ga [Wenzl 1978]. The angle in the case of Ga was measured both with He as the vapour phase and with an aqueous solution of HCl replacing the vapour phase (value not shown in Table 1.9). Additional similar measurements for Ge and Au are reported in [Wenzl 1978].

The direct viewing approach (method 1) was used in a number of additional investigations. The growth angle of sapphire was measured, using this method, by Satunkin and

Table 1.9 *Values of growth angles reported in the literature*

Material ^a	α (°)	Surface ^b	References	Method
Si {111}	11 ± 1	Nonfaceted	[Surek 1975]	2
	11 ± 1.5	Nonfaceted	[Hamidi 1983]	2
	11.4–19.9	Nonfaceted	[Antonov 2002] ^c	2
	12 ± 1	Unknown	[Satunkin 1980]	2
Si {110}	11 ± 1.5	Nonfaceted	[Hamidi 1983]	2
Si	12 ± 1	Isotropic	[Satunkin 2003]	2
	10	Isotropic	[Virozub 2008] ^d	2
	8.5–9	Polycrystalline	[Surek 1975]	2
	9.5 ± 1.5	Polycrystalline	[Hamidi 1983]	2
	15–20	Unknown	[Shashkov 1965]	1
Ge {111}	13 ± 1	Nonfaceted	[Surek 1975, 1976]	2
	12 ± 1	Facet	[Satunkin 2003]	2
Ge {110}	14 ± 1	Facet	[Satunkin 2003]	2
Ge	8	Polycrystalline	[Surek 1975]	2
	8–10.3	Polycrystalline	[Antonov 2002] ^c	2
	14 ± 1	Isotropic	[Satunkin 2003]	2
	12 ± 1	Isotropic	[Satunkin 1980]	2
	14.3	Isotropic	[Virozub 2008] ^d	2
	7 ± 3	Unknown	[Wenzl 1978]	1
InSb ($\bar{1}\bar{1}\bar{1}$)	25 ± 1	Facet	[Satunkin 1980]	2
	25.5 ± 0.5	Facet	[Antonov 2002] ^e	2
	25–30	Facet	[Satunkin 2003]	2
LiNbO ₃	0	Unknown	[Satunkin 1986]	1
NaNO ₂	7 ± 1	Unknown	[Ivantsov 1986]	1
LiF	19 ± 2	Unknown	[Ivantsov 1986]	1
Sapphire {0001}	35 ± 4	Facet	[Dreeben 1980]	1
Sapphire	17 ± 4	Nonfaceted periphery	[Dreeben 1980]	1
Sapphire	20 ± 5	Unknown	[Tatarchenko 1977]	1
Sapphire	12 ± 1	Unknown	[Satunkin 1980]	1
Cu	0	Nonfaceted	[Wenzl 1976]	1
Ga	0	Facet	[Wenzl 1978]	1
Au	0	Unknown	[Wenzl 1978]	1
GaP (111)	9.8 ± 0.5	Facet	[Antonov 2002]	2
InP (111)	7.0 ± 0.5	Facet	[Antonov 2002]	2
GaSb	30.7 ± 2	Unknown	[Tegetmeier 1996]	1
GaSb (μg)	28	Unknown	[Tegetmeier 1996]	1
W	20 ± 5	Unknown	[Glebovsky 1989]	1
GaAs	16	Unknown	[Satunkin 2003]	2

^aIn some cases the nominal orientation of the solid/liquid interface (i.e. the growth direction) is provided.

^bThis is the quality of the solid/liquid interface which, if reported, is typically known only at the onset of solidification.

^cBased on data from [Surek 1975].

^dBased on data from [Satunkin 2003].

^eBased on data from [Satunkin 1980].

co-workers [Tatarchenko 1977, Satunkin 1980]. The measurement system involved pulling thin crystalline rods through a shaper, where the growth angle was determined by a number of different analysis techniques applied to data on solid/vapour and liquid/vapour interfaces obtained by direct observation of the TPL and shaper regions. The

application of method 1 to sapphire growth is also reported in [Dreeben 1980], in which case the crystals were grown in a laser-heated float zone system. In [Satunkin 1986] Satunkin and co-workers emphasize the fact that their (type 1) method, applied to the pulling of thin lithium niobate rods from a shaper, does not require knowledge of the position of the TPL. The method described in [Satunkin 1986] is applicable to crystals of uniform diameter. The constant diameter assumption is also necessary when using the type 1 method applied in [Ivantsov 1986] for the determination of the growth angles of LiF and NaNO₂.

Two more studies involve the application of method 1 in the measurement of growth angles of W [Glebovsky 1989] and GaSb [Tegetmeier 1996]. The growth angle was determined in [Glebovsky 1989] using an approximate analytical solution for the meniscus between tube-shaped feed and crystalline rods in an electron-beam zone melting system. The analysis in [Tegetmeier 1996] involved fitting lines to the meniscus and solid/vapour interface to determine the growth angle in a floating zone system, both under normal conditions and in microgravity. Finally, an example of method 1 applied to the case of floating zone growth of Si can be found in Chapter 4 of this book.

The *a posteriori* analysis of solidified material (method 2) was, to the best of our knowledge, pioneered by Surek and Chalmers [Surek 1975]. These authors determined growth angle values based on a careful examination of a re-solidified small circular region of melt created in a thin crystalline wafer using an electron gun. Gravity was ignored in the analysis and the solid/liquid interface was assumed planar. This technique was applied to the case of Si and Ge [Surek 1975, Surek 1976], where in [Surek 1976] a rough estimate of gravitational effects was mentioned.

In [Satunkin 1980] Satunkin *et al.* presented a study of InSb, where the measurement was based on the *a posteriori* analysis of directionally solidified drops obtained when Czochralski-grown crystals were pulled free (i.e. separated) from the melt. The analysis involved approximating the solid/vapour interface to be parabolic in shape, an assumption of negligible effect of gravity on the liquid/vapour interface form, as well as a planar solid/liquid (growth) interface. Interestingly, in their later publication [Satunkin 1986], Satunkin and co-workers mentioned that transparent materials such as LiNbO₃ or sapphire cannot be analysed using this method since solidification in this case is not unidirectional from the base (original crystallization front) to the tip.

The method proposed in [Surek 1975] was used in [Hamidi 1983] to determine angles of Si both in vacuum and under Ar atmosphere. Antonov and Selin [Antonov 2002] proposed an elegant method for determining the growth angle from directionally solidified drops based on their cone angle and the assumptions of negligible gravitational effect on meniscus shape as well as a planar solidification front. This method was applied to GaP and InP systems as well as to photographs from the literature of InSb [Satunkin 1980], Ge [Surek 1975] and Si [Surek 1975]. Interestingly, the comparison with results of Surek [Surek 1975] was in some cases excellent in spite of the fact that the solidification geometry in [Surek 1975] is different from that of a solidifying drop.

An extensive report on measurements of growth angles using method 2 applied to Ge, Si and InSb is given in [Satunkin 2003]. A number of analysis techniques are applied. In particular, the assumption of constant growth angle is tested and is found to be valid for Si and Ge but not for InSb. Finally, in [Virozub 2008] method 2 was applied to data on Ge and Si drops from [Satunkin 2003] in a manner that requires no assumptions regarding

the shape of the solidification front. Once determined, the accuracy of the growth angle value and the possibility that it can be assumed constant were both verified using a detailed dynamic growth simulation involving coupled heat transport and capillarity. Results highlight the possible importance of gravity in these problems. In addition, this reference suggests that solidified drop shapes may not be very sensitive to the shape of the solid/liquid interface during growth.

Although (as can be seen in Table 1.9) several measurements were made on systems with a known crystallographic orientation, it is not always obvious if the solidification interface near or at the TPL is faceted or atomically rough. As can be understood from section 1.3.1 as well as from [Voronkov 1981, Satunkin 2003], although knowledge of the exact nature of the solid/liquid and solid/vapour interfaces at the TPL may not always be necessary for growth angle measurement, this information is important for the interpretation of measured values.

1.3.3 Application of the Growth Angle Condition in Simulations of Crystal Growth

Rigorous simulations of meniscus-defined crystal growth processes, in which the liquid/vapour interface shape is calculated, should be consistent with the growth angle as dictated by the application of the physics, described in section 1.3.1, to the system at hand. Relevant modelling efforts of melt growth systems, coupling heat transport and capillarity in a self-consistent manner, can be traced back to the mid 1980s. Some of the earliest studies include a quasi-steady-state model for the edge-defined film-fed (EFG) growth of Si [Ettouney 1983], a steady-state description of small-scale floating-zone growth of Si [Duranceau 1986] and a dynamic analysis of the Czochralski growth of Ge [Crowley 1983]. In [Ettouney 1983] the growth angle value is enforced as a boundary condition in the numerical solution of the Young–Laplace equation for the liquid/vapour interface shape, in [Duranceau 1986] this boundary condition is used to determine the *a priori* unknown pressure jump across the liquid/vapour interface, and in [Crowley 1983] the growth angle value is implemented by a dynamic equation relating the changing crystal diameter to the crystal growth rate at the TPL. This equation, important when considering the stability of growth (see Chapter 2 of this book) and control of crystal diameter (see [Hurle 1994] and Chapter 3), is given by:

$$\frac{dr_c}{dt} = v_g \tan(\psi - \alpha), \quad (1.29)$$

where r_c is the crystal radius at the TPL, ψ is the angle between the vertical and the liquid/vapour interface, and v_g is the crystal growth rate at the TPL; note that in Czochralski growth systems this growth rate is equal to the difference between the pull rate and the rate of change of melt height below the TPL.

It is interesting to note, that in the case of a floating zone system (discussed in [Duranceau 1986]), in which two TPLs exist, the growth angle is enforced only at the TPL associated with growth. No angles are specified at the TPL on the melting solid/vapour interface (i.e. on the feed rod). A relevant discussion of this issue is presented, in

relation to back-melting during Czochralski growth, in [Van den Bogaert 1996]. Following the discussion in this reference, it is probably best to restrict growth angle measurements to experiments in which it is verified that growth actually takes place at the relevant TPL.

The field of crystal growth modelling has advanced considerably since the mid-1980s. Highly sophisticated modelling efforts have been reported in the literature, many of which involve simulation of meniscus-defined systems in which transport-phenomena and capillarity are rigorously coupled. Physically consistent methods, accounting for the growth angle condition in these studies, are typically based on the principles laid down in the three above-mentioned references and other early works. A description of the development and application of relevant modelling efforts, which is beyond the scope of this chapter, is given in several review articles and book chapters published since the mid 1980s (e.g. [Brown 1988, Dupret 1994, Yeckel 2005]). In addition, note that a discussion related to the application of modelling to the floating zone technique can be found in Chapter 4 of this book.

1.3.3.1 Constant Growth Angle Approximation

Almost all of the computational analyses of meniscus-defined growth, accounting for the growth angle, assume it to be constant in both time and space. Exceptions include the analysis of a directionally solidifying sessile water drop [Anderson 1996] in which a dynamic angle was used to fit experimental data, and the calculation of a nonaxisymmetric cross-section of crystals pulled from the melt [Pet'kov 1993] which involved growth angle anisotropy in the plane perpendicular to the growth direction. However, in [Anderson 1996] heat transport was not accounted for in the analysis. As indicated in [Schultz 2001] and shown in [Virozub 2008], agreement with experimentally observed features in this particular case (involving solidification of a sessile water drop) can be obtained when heat transport is accounted for in the analysis without the need for relaxing the constant growth angle approximation. In addition, although the basic reasoning behind the analysis in [Pet'kov 1993] is sound, this two-dimensional study is limited to the cross-sectional plane of the crystal with no account for heat transport in the formulation.

In [Virozub 2008] a method is discussed for the estimation and verification of growth angle values based on experimentally obtained directionally solidified sessile or pendant drops. The estimation refers to the angle exhibited at the initial stages of drop solidification while the verification is based on the constant growth angle assumption. The two examples shown in this reference, of Si and Ge solidifying on isotropic fronts of Czochralski-grown crystals pulled free from the melt, suggest that this assumption is satisfactory in these systems. Following the discussion in section 1.3.1, it is theoretically possible for this assumption to fail in systems exhibiting anisotropy of interfacial energies, significant undercooling at the TPL, or a combination of both. It is important to note however, that even in cases where one or both of these phenomena occur, the angle may still remain constant throughout growth due to *time-independent* conditions at the TPL. Finally, as discussed above in relation to [Pet'kov 1993], three-dimensional effects, such as those involving anisotropy of interfacial energies in the plane perpendicular to the growth direction, may lead to nonuniform growth angle values along the TPL.

The following involves the application of an approach based on the method presented in [Virozub 2008], further probing issues related to the constant growth angle

approximation. In particular a situation is examined, where a facet dominates the solid/liquid interface. Since the method and related equations are given in detail in [Virozub 2008], they are only briefly mentioned here. Additional information, associated with anisotropic interfacial attachment growth kinetics, is briefly discussed below with more detail provided in [Weinstein 2004].

Computational Approach to the Estimation and Verification of Growth Angle Values. Our starting point is a solidified pendant or sessile drop whose shape, which is known, is used for the determination of the solid drop volume as well as the angle of contact between the solid/vapour interface and the substrate. The solidified material volume is multiplied by the solid-to-liquid density ratio thus providing a value for the original liquid drop volume. This is then used, together with the known drop/substrate (circular) interfacial area, to determine the liquid drop's shape by numerical solution of the Young–Laplace equation with gravity (see Chapter 8 for the various forms of the Young–Laplace equation):

$$\frac{1}{r} \frac{d}{dr} \left\{ r \frac{dz_l}{dr} \left[1 + \left(\frac{dz_l}{dr} \right)^2 \right]^{-1/2} \right\} = \frac{\rho_l (z_{la} - z_l)}{\gamma_{lv}} (\mathbf{g} \cdot \mathbf{e}_z) - \frac{2}{b} \quad (1.30)$$

The coordinate system used here is the same as the one described below (see Figure 1.25) in the context of drop-solidification calculations, where $z_l(r)$ is the z -coordinate value of the liquid/vapour interfacial profile at a given radial position. In Equation (1.30) $1/b$ is the drop's mean curvature at its apex ($r = 0$, $z_l = z_{la}$), z_{la} is the vertical distance of the drop apex from its base, \mathbf{e}_z is the unit vector in the z coordinate direction and \mathbf{g} is the gravity vector. Boundary conditions applied in this case are a symmetry (zero slope) condition at $r = 0$ and the fact that, at $r = R_0$, the liquid/vapour interface's vertical position is fixed at $z_l = 0$. In addition, the parameter $1/b$ is determined by coupling the solution of Equation (1.30) with that of an additional equation enforcing the pre-determined liquid

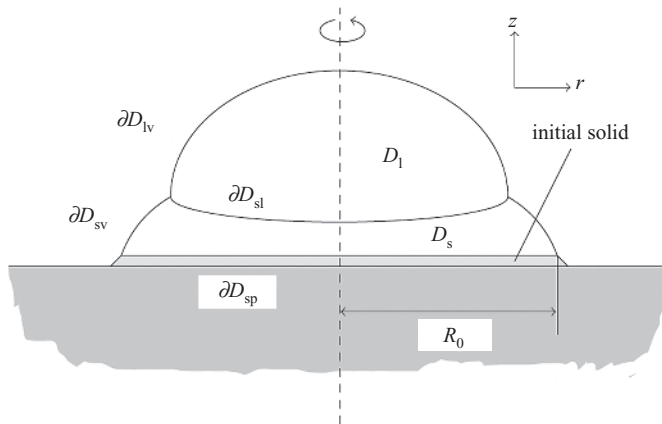


Figure 1.25 Mathematical representation of model system for drop solidification.

volume. Once the shape, $z_i(r)$, is known it is possible to evaluate the angle of contact between the liquid/vapour interface and the substrate. Finally, the difference between this angle and the previously obtained contact angle of the solidified drop is the estimated growth angle.

Verification of the estimated growth angle, assuming it is constant, is obtained by solving the coupled problem of heat transport, phase-change and capillarity during the directional solidification of the drop. A mathematical representation of the axially-symmetric model system used in these calculations is shown in Figure 1.25.

The evolution of the temperature field in the solid (D_s) and liquid (D_l) phases during solidification is assumed to be governed by the heat equation:

$$\rho_i C_{pi} \frac{\partial T}{\partial t} = \nabla \cdot k_i \nabla T \quad (i = l, s), \quad (1.31)$$

where ρ_i , C_{pi} , and k_i are, respectively, the density, heat capacity and thermal conductivity of phase i , while T , t and ∇ represent temperature, time and the gradient operator. Note that in this analysis of small-scale systems with relatively low-valued temperature gradients, we have neglected the impact, on the thermal field, of melt flow driven either by buoyancy or by surface tension gradients.

External boundary conditions for this problem include a prescribed ($T = T_0$) temperature along the interface between the drop and the cold substrate (∂D_{sp}) and heating by the environment at the liquid/vapour (∂D_{lv}) and solid/vapour (∂D_{sv}) interfaces according to:

$$-k_i \nabla T \cdot \mathbf{n}_{ij} = h(T - T_a) \quad (ij = lv, sv), \quad (1.32)$$

where \mathbf{n}_{ij} is the unit normal vector pointing from the interface towards the environment, T_a is the ambient temperature and h is the convective heat transfer coefficient enhanced due to radiative transport effects.

Along the solidification interface (∂D_{sl}) a balance of heat fluxes requires adherence to the Stefan condition given by:

$$[(k_s \nabla T)_s - (k_l \nabla T)_l] \cdot \mathbf{n}_{sl} = \Delta H v_n, \quad (1.33)$$

where the subscripts l and s respectively denote quantities evaluated on the liquid and solid sides of the solid/liquid interface, the volumetric heat of fusion is given by ΔH , v_n is the normal growth rate and \mathbf{n}_{sl} is the unit normal vector pointing from the interface into the liquid phase. In [Virozub 2008] the solid/liquid interface is assumed to coincide with the melting point isotherm. This assumption, which is consistent with extremely fast interfacial attachment growth kinetics, is relaxed (where necessary) in the following to allow for the formation of a kinetically driven facet during solidification; see e.g. [Weinstein 2004] for a full discussion of our approach to the problem of faceting. In this case, the simple isotherm condition ($T = T_m$ on ∂D_{sl}) in [Virozub 2008] is replaced here by the more general equation:

$$v_n = \beta_k \Delta T, \quad (1.34)$$

where ΔT is the undercooling on ∂D_{sl} and β_k is the kinetic coefficient (which is not necessarily constant). In the common event of an atomically rough solid/liquid interface, kinetics of growth are extremely fast (β_k is relatively large), the resultant undercooling value is negligible ($\Delta T \rightarrow 0$), and the isotherm condition used in [Virozub 2008] is recovered. However, when (at some point on the solid/liquid interface) crystal growth occurs along a singular orientation, a facet may appear, molecular attachment kinetics become relatively slow and the resultant nonnegligible undercooling must be accounted for. This is done via Equation (1.34) where the kinetic coefficient now depends on the undercooling as well as on the deviation from the singular orientation (δ), in accordance with basic crystal growth mechanisms characteristic of growth in the vicinity of an atomically smooth singular surface.

As described in detail in [Weinstein 2004], a general expression for the kinetic coefficient near a singular surface can be formulated using a combination of the following expressions:

$$\beta_k(\Delta T, \delta) = \begin{cases} \beta_r & \text{rough surface} \\ \beta_{st} |\sin \delta| & \text{vicinal surface} \\ C(\cos \delta) \Delta T & \text{screw dislocation} \\ B(\cos \delta) e^{-A/\Delta T} & \text{two-dimensional nucleation} \end{cases} \quad (1.35)$$

where β_r is a large-valued rough growth kinetic coefficient (practically enforcing the isotherm condition), β_{st} is a step kinetic coefficient and A , B and C are additional parameters which, together with β_r and β_{st} , can be treated as constants. In the most simple (yet robust) approximation, each mechanism is enforced separately depending on the local crystallographic orientation and (in the case of extremely small values of δ) on the nature of the singular surface. For large enough values of δ rough surface kinetics are used, for intermediate δ values vicinal kinetics are enforced, and below a certain value of δ either screw dislocation or two-dimensional nucleation kinetics are applied depending on the availability of screw dislocations on the surface. In [Weinstein 2004] (and here) the crossover from step source (screw dislocation or two-dimensional nucleation) to vicinal surface kinetics for $\langle 111 \rangle$ Si is modelled as occurring at misorientation values on the order of 0.001° , while switching to rough growth kinetics is enforced at δ values on the order of 0.5° .

The liquid/vapour interface shape is calculated, as a function of time, by solving Equation (1.30) coupled with an overall mass conservation equation for the determination of l/b , where a zero interfacial slope condition is imposed at the liquid drop's apex and the edge of the drop is positioned to coincide with the TPL. Finally, self-consistency with the thermal field calculation is enforced by applying the growth angle condition according to which α is equal to the difference between the inverse tangent (arctan) values of the solid/vapour and liquid/vapour interfacial slopes at the TPL.

The finite-element based numerical procedures for solution of the equations presented above are mostly given in [Virozub 2008]. When enforcing the isotherm condition (as in [Virozub 2008]), an iterative procedure is used, involving an empirically determined interface motion coefficient. However, when modelling a solid/liquid interface which exhibits a facet, this interface motion procedure is replaced with the algorithm described

in detail in [Weinstein 2004]. Details of mesh and time-step sizes as well as other numerical parameters are the same as in [Virozub 2008] except for when Equation (1.34) is applied. In this case a reduced time-step size ($\Delta t = 0.00025$ s) is used with approximately 70 substeps employed for advancement of the interface at each time-step.

As already discussed above, in [Virozub 2008] the growth angles for Si and Ge were estimated (and verified to be constant), based on experiments reported in [Satunkin 2003]. Here additional data from [Satunkin 2003] is used to estimate the growth angle for InSb ($\bar{1}\bar{1}\bar{1}$). The resultant growth angle value, obtained using the procedure briefly described above (and in more detail in [Virozub 2008]), is found to be given by $\alpha = 25^\circ$. Next the verification procedure is applied while assuming the isotherm condition to be applicable (i.e. ignoring effects of interface attachment kinetics). System parameters and physical coefficients are given, respectively, by the following values of estimated base undercooling, estimated ambient overheating, liquid density [Kozhemyakin 1995], solid density [Vaidya 2006], heat of fusion [Vaidya 2006], solid conductivity [Vaidya 2006], liquid conductivity [Roussopoulos 2004], volumetric liquid heat capacity [Kozhemyakin 1995], volumetric solid heat capacity [Vaidya 2006], liquid/vapour interfacial energy [Hurle 1995] and estimated heat transfer coefficient: $T_m - T_0 = 10$ K, $T_a - T_m = 12$ K, $\rho_l = 6430$ kg/m³, $\rho_s = 5640$ kg/m³, $\Delta H = 1.3 \times 10^9$ J/m³, $k_s = 4.57$ W/mK, $k_l = 12.3$ W/mK, $\rho_l C_{pl} = 1.68 \times 10^6$ J/m³K, $\rho_s C_{ps} = 1.5 \times 10^6$ J/m³K, $\gamma_v = 0.434$ J/m², $h = 115$ W/m²K.

A plot of the predicted solidified drop profile, obtained with the above estimated angle value, is shown in Figure 1.26 together with the relevant experimental data from [Satunkin 2008]. For comparison, this figure contains a similar plot for the case of Ge grown on an isotropic growth front, obtained using the angle $\alpha = 14.3^\circ$ which was determined and verified in [Virozub 2008]. The agreement between experiment and simulation is excellent, suggesting that the growth angle is indeed constant. However, in the case of InSb, numerical difficulties limited the ability to simulate solidification beyond the level shown in Figure 1.26. Consider the nonnegligible size of the residual liquid drop in this case ($\sim 4\%$ of original volume as compared with less than 0.5% in the case of Ge). It is theoretically possible that, if achievable, continued simulated solidification may reveal a discrepancy between experimental and simulated profiles for small values of the radial coordinate. It is important to consider this possibility in this case since Satunkin’s analysis

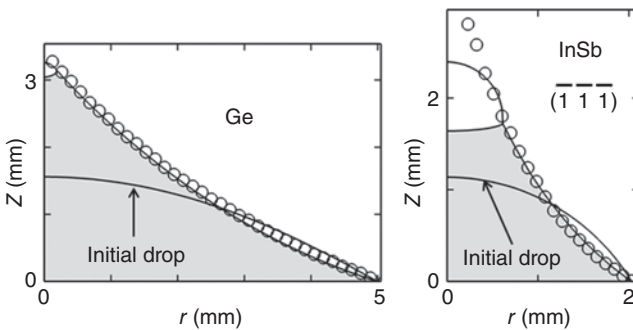


Figure 1.26 Experimental (circles) and simulated (solid lines) directionally solidified pendant drop profiles. Shaded regions are the final (simulated) solid drop shapes. The small regions above the simulated solid drops are the residual liquid.

[Satunkin 2003] determined the growth angle of this material to be nonconstant (see Table 1.9). In addition, as mentioned above, the verifications exhibited in Figure 1.26 were made using the isotherm condition at the interface. Strictly speaking, this approach is incorrect in the event (possibly relevant in the case of InSb shown in Figure 1.26) that a facet appears on the solid/liquid interface during the solidification process.

The importance of using the rigorous boundary condition, Equation (1.34), in cases involving facets at the solid/liquid interface is investigated using a hypothetical case of Si drop solidification in the $\langle 111 \rangle$ direction. Here parameters are the same as those used in [Virozub 2008] for the case of Si growing on an isotropic growth front. Since the actual value of the growth angle is not truly known in this case, the same value ($\alpha = 10^\circ$) as that determined in [Virozub 2008], is chosen. Solidification is simulated twice. First an analysis identical to that employed in [Virozub 2008] is applied. Next, the solidified drop profile is recalculated, this time using the rigorous approach involving Equation (1.34) which accounts for interface attachment kinetics on a facet, should it evolve. In this case it was assumed that a two-dimensional nucleation mechanism dominates step generation. Parameters relevant to Equation (1.35) are $\beta_l = 0.001$ m/sK, $\beta_{sl} = 0.63$ m/sK, $B = 4.8 \times 10^8$ m/sK and $A = 140$ K. Looking at the results, shown in Figure 1.27, it is interesting to note that, although the more rigorous calculation predicts the solid/liquid interface to be dominated by a $\{111\}$ facet, this result has almost no impact on the shape of the solidified drop. This suggests that the commonly used approach of assuming the solid/liquid interface to be planar, when estimating the growth angle, may yield accurate results even in some of the cases where this assumption is clearly incorrect. Additional calculations (not exhibited here), showing a surprising insensitivity of the solidified drop shape to variations in k_s , k_l , h , T_0 and T_a , provide further support for this conclusion at least with respect to the Si system considered here.

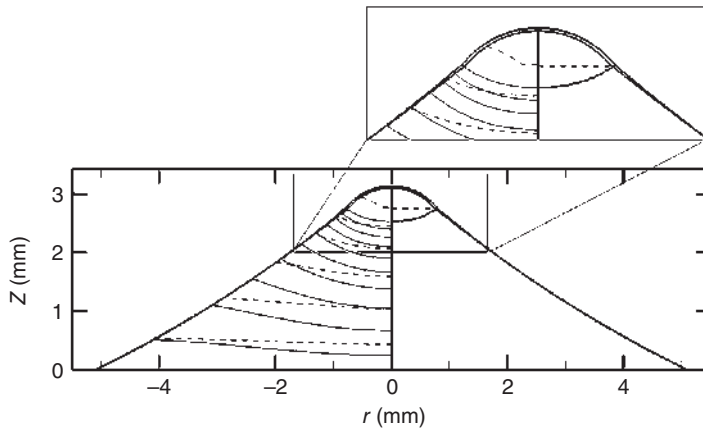


Figure 1.27 Thermal fields and interfacial profiles during simulated solidification of Si in the $\langle 111 \rangle$ direction assuming $\alpha = 10^\circ$. Right-hand side (both of main figure and of inset) depicts solid/vapour, residual liquid/vapour and solid/liquid interfacial profiles; the dashed line demarks the solid/liquid interface when faceting is accounted for. Left-hand side depicts isotherms spaced 1K apart. Dashed lines correspond to the faceted growth calculation and solid lines to those obtained using the isotherm condition.

1.3.4 Summary

The concept of the growth angle, its measurement and relevant crystal growth simulations are reviewed. The constant growth angle approximation appears valid in cases where significant anisotropy is not present near the TPL. The existence of a facet (associated with significant anisotropy) at or near the TPL may lead to variations in the value of the growth angle. However, if steady-state growth conditions are maintained near the TPL, this growth angle value may remain constant throughout most of the solidification process.

The agreement between different measurements of growth angle values for a given material is not always satisfactory (see Table 1.9). There may be a number of reasons for the discrepancies. Although some of the relevant references include information on the quality of the solid/liquid interface (faceted, polycrystalline, nonfaceted), it is not necessarily simple to verify that this information is accurate throughout the solidification process. In particular, the quality of the interface at the TPL (e.g. the nature of contact between a solid/liquid interfacial facet and the TPL) is not easy to resolve. An additional complication is related to the accuracy of the estimation methods employed. Systematic errors may be introduced due to the use of approximate solutions of relevant equations. For example, as shown in [Virozub 2008], when neglecting the effect of gravity in the analysis of solidifying drops it is important to make sure that the Bond number is small (to be on the safe side it is probably best to neglect gravity only when $Bo < 0.1$). Assuming the solid/liquid interface to be planar when calculating solidification profiles is probably incorrect in many cases considered in the growth angle measurement literature. However, the rigorous growth angle verification procedure, applied here for a hypothetical case of a $\langle 111 \rangle$ Si drop solidification process, shows almost no change in the solidification profile when simulating a faceted (flat) as compared to a curved (non-faceted) solid/liquid interface (using the same value of the growth angle in both cases). Further manipulation of system parameters indicates that the solidification profile is, in this case, relatively insensitive to heat transport. This result, which is in contradiction with the situation described for solidification of a sessile water drop ([Virozub 2008] as compared with [Anderson 1996]), suggests that a more complete investigation of this issue is necessary.

Anisotropy and the possibility of a nonconstant growth angle are important issues which require further attention. Understanding the three-dimensional picture of a meniscus-defined growth process often requires the consideration of anisotropy in the plane of solidification (along the TPL). The coupling of capillarity with kinetics associated with faceted growth near the TPL in relevant systems (see e.g. [Santos 1996]), is a nontrivial problem which must be addressed when considering the three-dimensional analysis of such processes.

Acknowledgements

S.B. and A.V. thank G.A. Satunkin for providing them with original versions of the photographs exhibited in [Satunkin 2003] and would also like to thank Dr I.G. Rasin for his assistance in resolving numerical problems.

References

- [Anderson 1996] Anderson D.M., Grae Worster M., Davis S.H., *J. Cryst. Growth* **163** (1996) 329.
- [Antonov 1965] Antonov P.I., *Sb. Rost. Kristallov.* **6** (1965) 158 (Consultants Bureau Report No. IRN1031619X).
- [Antonov 2002] Antonov V.A., Selin V.V., *J. Cryst. Growth* **241** (2002) 507.
- [Bardsley 1974] Bardsley W., Frank F.C., Green G.W., Hurle D.T.J., *J. Cryst. Growth* **23** (1974) 341.
- [Barsoum 1981] Barsoum M.W., Ownby P.D., In: *Surfaces and Interfaces in Ceramic and Ceramic-Metal Systems*, Materials Science Research, Volume 14, ed. J. Pask and A. Evans, Plenum Press, New York (1981), pp. 457–466.
- [Baumli 2008] Baumli P., Kaptay G., *Mater. Sci. Eng. A* **495** (2008) 192–196.
- [Blake 1993] Blake T.D., In: *Wettability*, ed. J.C. Berg, Marcel Dekker, New York (1993), pp. 251–309.
- [Bohm 1994] Bohm J., Lüdge A., Schröder W., In: *Handbook of Crystal Growth Vol. 2a – Bulk Crystal Growth: Basic Techniques*, ed. D.T.J. Hurle, North Holland, Amsterdam (1994), pp. 213–257.
- [Boiton 1999] Boiton P., Giacometti N., Duffar T., Santailier J.L., Dusserre P., Nabot J.P., *J. Cryst. Growth* **206** (1999) 159–165.
- [Brown 1988] Brown R.A., *AIChE J* **34**(6) (1988) 881.
- [Cassie 1948] Cassie A.B.D., *Discuss. Faraday Soc.* **3** (1948) 11–16.
- [Castello 1994] Castello P., Ricci E., Passerone A., Costa P., *J. Mater. Sci.* **29** (1994) 6104–6114.
- [Champion 1973] Champion J.A., Keene B.J., Allen S., *J. Mater. Sci.* **8** (1973) 423–426.
- [Chizhik 1985] Chizhik S.P., Gladkikh N.T., Larin V.I., Grigor'eva L.K., Dukarov S.V., Stepanova S.V., *Poverkhnost* **12** (1985) 111–121 (in Russian).
- [Cobb 1999] Cobb S.D., Szofran F.R., Jones K.S., Lehoczy S.L., *J. Electron. Mater.* **28** (1999) 732–739.
- [Cox 1986] Cox R.G., *J. Fluid Mech.* **168** (1986) 169–194.
- [Cröll 2002] Cröll A., Salk N., Szofran F.R., Cobb S.D., Volz M.P., *J. Cryst. Growth* **242** (2002) 45–54.
- [Cröll 2003] Cröll A., Lantzsch R., Kitanov S., Salk N., Szofran F.R., Tegetmeier A., *Cryst. Res. Technol.* **38** (2003) 669–675.
- [Crowley 1983] Crowley A.B., *IMA J. Appl. Math.* **30** (1983) 173.
- [de Gennes 1985] de Gennes P.G., *Rev. Modern Phys.* **57** (1985) 827–863.
- [de Gennes 2004] de Gennes P.G., Brochard-Wyart F., Quéré D., *Capillarity and Wetting Phenomena: Drops, Bubbles, Pearls, Waves*, Springer, New York (2004).
- [Dezellus 1999] Dezellus O., Eustathopoulos N., *Scripta Mater.* **40** (1999) 1283–1288.
- [Dezellus 2000] Dezellus O., PhD thesis, INP-Grenoble, France (2000) (in French).
- [Dezellus 2005] Dezellus O., Jacques S., Hodaj F., Eustathopoulos N., *J. Mater. Sci.* **40** (2005) 2307–2311.
- [Dreeben 1980] Dreeben A.B., Kim K.M., Schujko A., *J. Cryst. Growth* **50** (1980) 126.
- [Drevet 2009] Drevet B., Voytovych R., Israel R., Eustathopoulos N., *J. Eur. Ceram. Soc.* **29** (2009) 2363–2367.
- [Duffar 1997] Duffar T., Boiton P., Dusserre P., Abadie J., *J. Cryst. Growth* **179** (1997) 397.
- [Duffar 2009] Duffar T., Bochu O., Dusserre P., *J. Mater. Sci.*, DOI: 10.1007/s10853-009-4041-3
- [Dupré 1869] Dupré A., *Théorie Mécanique de la Chaleur*, Chapter IX, Gauthier-Villars, Paris (1869).
- [Dupret 1994] Dupret F., Van den Bogaert N., In: *Handbook of Crystal Growth, Vol. 2b – Bulk Crystal Growth: Growth Mechanisms and Dynamics*, ed. D.T.J. Hurle, North Holland, Amsterdam (1994), pp. 875–1010.
- [Duranceau 1986] Duranceau J.L., Brown R. A., *J. Cryst. Growth* **75** (1986) 367.
- [Ellefson 1938] Ellefson B.S., Taylor N. W., *J. Am. Ceram. Soc.* **21** (1938) 193–205.

- [Ettouney 1983] Ettouney H.M., Brown R.A., Kalejs J.P., *J. Cryst. Growth* **62** (1983) 230.
- [Eustathopoulos 1998] Eustathopoulos N., Drevet B., *Mater. Sci. Eng. A* **249** (1998) 176–183.
- [Eustathopoulos 1999] Eustathopoulos N., Drevet B., Nicholas M., *Wettability at High Temperatures*, Pergamon, Oxford (1999).
- [Eustathopoulos 2001] Eustathopoulos N., Drevet B., Muolo M.L., *Mater. Sci. Eng. A* **300** (2001) 34–40.
- [Eustathopoulos 2005a] Eustathopoulos N., Sobczak N., Passerone A., Nogi K., *J. Mater. Sci.* **40** (2005) 2271–2280.
- [Eustathopoulos 2005b] Eustathopoulos N., *Curr. Opin. Solid State Mater. Sci.* **9** (2005) 152–160.
- [Flemings 1974] Flemmings M.C., *Solidification Processing*, McGraw-Hill, New York (1974).
- [Garandet 1998] Garandet J.P., Drevet B., Eustathopoulos N., *Scripta Mater.* **38** (1998) 1391–1397.
- [Glebovsky 1989] Glebovsky V.G., Semenov V.N., Lomeyko V.V., *J. Cryst. Growth* **98** (1989) 487.
- [Hamidi 1983] Hamidi M., Rodot H., *Rev. Phys. Appl.* **18** (1983) 75.
- [Harter 1993] Harter I., Dusserre P., Duffar T., Nabot J.P., Eustathopoulos N., *J. Cryst. Growth* **131** (1993) 157–164.
- [Herring 1951] Herring C., In: *The Physics of Powder Metallurgy*, ed. W.E. Kingston, McGraw-Hill, New York (1951), pp. 143–179.
- [Hitchcock 1981] Hitchcock S.J., Carroll N.T., Nicholas M.G., *J. Mater. Sci.* **16** (1981) 714–732.
- [Hoffman 1972] Hoffman D.W., Cahn J.W., *Surf. Sci.* **31** (1972) 368.
- [Hurle 1994] Hurle D.T.J., Cockayne B., In: *Handbook of Crystal Growth Vol. 2a – Bulk Crystal Growth: Basic Techniques*, ed. D.T.J. Hurle, North Holland, Amsterdam (1994), pp. 99–211.
- [Hurle 1995] Hurle D.T.J., *J. Cryst. Growth* **147** (1995) 239.
- [Ivantsov 1986] Ivantsov V.A., Antonov P.I., Panov M.F., USSR. Mat. Vses. Soveshch. Poluch. Profilirovannykh Krist. Izdelii Sposobom Stepanova Ikh Primen. Nar. Khoz. (1986), Meeting Date 1985, pp. 138–142 (in Russian).
- [Jaworske 1989] Jaworske D.A., Perry W.D., *AIAA 24th Thermophysics Conference*, Buffalo, NY, 12–14 June 1989, *AIAA-89-1756*, (1989).
- [Johnson 1993] Johnson R.E., Dettre R.H., In: *Wettability*, ed. J.C. Berg, Marcel Dekker, New York (1993), pp. 1–73.
- [Kaiser 2001] Kaiser N., Cröll A., Szofran F.R., Cobb S.D., Benz K.W., *J. Cryst. Growth* **231** (2001) 448–457.
- [Katty 1992] Katty A., Dusserre P., Triboulet R., Duffar T., *J. Cryst. Growth* **118** (1992) 470–472.
- [Kinoshita 1989] Kinoshita K., Yamada T., *J. Cryst. Growth* **96** (1989) 953–956.
- [Kistler 1993] Kistler S.F., In: *Wettability*, ed. J.C. Berg, Marcel Dekker, New York (1993), pp. 311–429.
- [König 1983] König U., Keck W., *J. Electrochem. Soc.* **130** (1983) 685.
- [König 1984] König U., Keck W., Kricks A., *J. Cryst. Growth* **68** (1984) 545–549.
- [Kozhemyakin 1995] Kozhemyakin G., *J. Cryst. Growth* **149** (1995) 266.
- [Kuandykov 2001] Kuandykov L.L., Antonov P.I., *J. Cryst. Growth* **222** (2001) 852.
- [Laplace 1805] Laplace P.S. (Marquis), *Traité de Mécanique Céleste*, Vol. 4, first section (théorie de l'action capillaire) of the supplement to book 10 (sur divers points relatifs au système du monde), Chez Courcier, Paris (1805), (in French).
- [Laurent 1988] Laurent V., Chatain D., Chatillon C., Eustathopoulos N., *Acta Metall.* **36** (1988) 1797–1803.
- [Li 1989] Li J.G., Coudurier L., Eustathopoulos N., *J. Mater. Sci.* **24** (1989) 1109–1116.
- [Maeda 1986] Maeda Y., Yokoyama T., Hide I., Matsuyama T., Sawaya K., *J. Electrochem. Soc.*, **133** (1986) 440–443.
- [Mailliar 2008] Mailliar O., Hodaj F., Chaumat V., Eustathopoulos N., *Mater. Sci. Eng. A* **495** (2008) 174–180.
- [Merlin 1992] Merlin V., PhD thesis, INP-Grenoble, France (1992) (in French).

- [Morel 1970] Morel C.F., *Surface Tensions of Molten Salts and Contact Angle Measurements of Molten Salts on Solids*, EUR 4482e, Commission of the European Communities–Euratom, Joint Nuclear Research Centre, Petten Establishment, Netherlands (1970).
- [Mortensen 1997] Mortensen A., Drevet B., Eustathopoulos N., *Scripta Mater.* **36** (1997) 645–651.
- [Mullins 1957] Mullins W.W., *J. Appl. Phys.* **28** (1957) 333–339.
- [Mullins 1960] Mullins W.W., *Trans. Met. Soc. AIME* **218** (1960) 354–361.
- [Naidich 1968] Naidich Y.V., Kolesnichenko G.A., *Russ. Metall.* **4** (1968) 141–149.
- [Naidich 1981] Naidich Y.V., In: *Progress in Surface and Membrane Science*, Vol. 14, ed. D.A. Cadenhead and J.F. Danielli, Academic Press, New York (1981), pp. 353–484.
- [Naidich 1992] Naidich Y.V., Sabuga W., Perevertailo V., *Adgeziya Raspl. Pajka Mat.* **27** (1992) 23–34 (in Russian).
- [Naidich 1995] Naidich J.V., Taranets N.Y., *Proc. 1st Int. Conf. High Temperature Capillarity*, Smolenice Castle, 8–11 May 1994, ed. N. Eustathopoulos (Reprint, Bratislava, 1995), pp. 138–142.
- [Neumann 1972] Neumann A.W., Good R.J., *J. Colloid Interface Sci.* **38** (1972) 341–358.
- [Nolfi 1972] Nolfi F.V., Johnson C.A., *Acta Metall.* **20** (1972) 769–778.
- [Ownby 1995] Ownby P.D., Weirauch D.A., Lazaroff J.E., *Proc. 1st Int. Conf. High Temperature Capillarity*, Smolenice Castle, 8–11 May 1994, ed. N. Eustathopoulos (Reprint, Bratislava, 1995), pp. 330–334.
- [Pech 2004] Pech J., Braccini M., Mortensen A., Eustathopoulos N., *Mater. Sci. Eng. A* **384** (2004) 117–128.
- [Pech 2005] Pech J., Berthomé G., Jeymond M., Eustathopoulos N., *Glass Sci. Technol.* **78** (2005) 54–62.
- [Pet'kov 1993] Pet'kov I.S., Red'kin B.S., *J. Cryst. Growth* **131** (1993) 598.
- [Roussopoulos 2004] Roussopoulos G., Rubini P., *J. Crystal Growth* **271** (2004) 333.
- [Saiz 1998] Saiz E., Tomsia A.P., Cannon R.M., *Acta Mater.* **46** (1998) 2349–2361.
- [Sangiorgi 1995] Sangiorgi R., Muolo M.L., Eustathopoulos N., *Proc. 1st Int. Conf. High Temperature Capillarity*, Smolenice Castle, 8–11 May 1994, ed. N. Eustathopoulos (Reprint, Bratislava, 1995), pp. 148–154.
- [Santos 1996] Santos M.T., Marin C., Diéguez E., *J. Cryst. Growth* **160** (1996) 283.
- [Satunkin 1980] Satunkin G.A., Tatartchenko V.A., Shaitanov V.I., *J. Cryst. Growth* **50** (1980) 133.
- [Satunkin 1986] Satunkin G.A., Red'kin B.S., Kurlov V.N., Rossolenko S.N., Tatartchenko V.A., Tufin Yu.A., *Cryst. Res. Technol.* **21** (1986) 995.
- [Satunkin 2003] Satunkin G.A., *J. Cryst. Growth* **255** (2003) 170.
- [Schultz 2001] Schultz W.W., Grae Worster M., Anderson D.M., In: *Interactive Dynamics of Convection and Solidification*, ed. P. Ehrhard, D.S. Riley, P.H. Steen, Kluwer, Dordrecht (2001), pp. 209–226.
- [Shashkov 1965] Shashkov Yu. M., Mel'nikov E.V., *Russ. J. Phys. Chem.* **39** (10) (1965) 1364.
- [Shetty 1990a] Shetty R., Balasubramanian R., Wilcox W. R., *J. Cryst. Growth* **100** (1990) 51–57.
- [Shetty 1990b] Shetty R., Balasubramanian R., Wilcox W. R., *J. Cryst. Growth* **100** (1990) 58–62.
- [Shi 1980] Shi Z.J., He Z.G., Ying C.F., *Ultrasonics* **18** (1980) 57–60.
- [Shimizu 2002] Shimizu A., Nishizawa J., Oyama Y., Suto K., *J. Cryst. Growth* **237–239** (2002) 1697–1700.
- [Shuttleworth 1950] Shuttleworth R., *Proc. Phys. Soc.* **A63** (1950) 444–457.
- [Smith 1948] Smith C.S., *Trans. AIME* **175** (1948) 15–51.
- [Surek 1975] Surek T., Chalmers B., *J. Cryst. Growth* **29** (1975) 1.
- [Surek 1976] Surek T., *Scripta Met.* **10** (1976) 425.
- [Tanaka 1996] Tanaka T., Hack K., Iida T., Hara S., *Z. Metallkd.* **87** (1996) 380–389.
- [Tatarchenko 1977] Tatarchenko V.A., Satunkin G.A., *J. Cryst. Growth* **37**(3) (1977) 285.
- [Tegetmeier 1996] Tegetmeier A., Cröll A., Danilewsky A., Benz K.W., *J. Cryst. Growth* **166** (1996) 651.

- [Towers 1954] Towers H., *Br. Ceram. Soc. Trans.* **53** (1954) 180–202.
- [Vaidya 2006] Vaidya N., Huang H., Liang D., *Comm. Comp. Phys.* **1** (3) (2006) 511.
- [Van den Bogaert 1996] Van den Bogaert N., Dupret F., *J. Cryst. Growth* **166** (1996) 446.
- [Virozub 2008] Virozub A., Rasin I.G., Brandon S., *J. Cryst. Growth* **310** (2008) 5416.
- [Voronkov 1963] Voronkov V.V., *Fizika Tverdogo Tela* **5** (2) (1963) 571 (in Russian; English translation *Sov. Phys. Solid State* **5** (2) (1963) 415).
- [Voronkov 1974] Voronkov V.V., *Krystallografiya* **19** (1974) 922 (in Russian; English translation *Sov. Phys. Crystallogr* **19** (5) (1975) 573).
- [Voronkov 1975] Voronkov V.V., Pankov V.M., *Krystallografiya* **20** (1975) 1145 (in Russian; English translation *Sov. Phys. Crystallogr* **20** (6) (1975) 697).
- [Voronkov 1978] Voronkov V.V., *Krystallografiya* **23** (1978) 249 (in Russian; English translation *Sov. Phys. Crystallogr.* **23** (2) (1978) 137).
- [Voronkov 1980] Voronkov V.V., *Izv. Akad. Nauk. SSSR, Ser. Fiz.* **44** (2) (1980) 226 (in Russian).
- [Voronkov 1981] Voronkov V.V., *J. Cryst. Growth* **52** (1981) 311.
- [Weinstein 2004] Weinstein O., Brandon S., *J. Cryst. Growth* **268** (2004) 299.
- [Wenzel 1936] Wenzel R.N., *Ind. Eng. Chem.* **28** (1936) 988–994.
- [Wenzl 1976] Wenzl H., Fattah A., Uelhoff W., *J. Cryst. Growth* **36** (1976) 319.
- [Wenzl 1978] Wenzl H., Fattah A., Gustin D., Mihelcic M., Uelhoff W., *J. Cryst. Growth* **43** (1978) 607.
- [Wery 2008] Wery S., PhD thesis, Université de Perpignan, France (2008) (in French).
- [Yasuda 1990] Yasuda K., Iwakami Y., Saji M., *J. Cryst. Growth* **99** (1990) 727–730.
- [Yeckel 2005] Yeckel A., Derby J.J., In: *Bulk Crystal Growth of Electronic, Optical and Optoelectronic Materials*, ed. P. Capper, John Wiley & Sons Ltd., Chichester (2005) pp. 73–119.
- [Young 1805] Young T., *Phil. Trans. R. Soc. Lond.* **94** (1805) 65–87.
- [Yuan 2004] Yuan Z., Huang W.L., Mukai K., *Appl. Phys. A* **78** (2004) 617–622.
- [Yuferev 2005] Yuferev V.S., Krymov V.M., Kuandykov L.L., Bakholdin S.I., Nosov Yu.G., Shulpina I.L., Antonov P.I., *J. Cryst. Growth* **275** (2005) e785.

